

Simulating Non-Markovian Open Quantum Dynamics with Neural Quantum States

Long Cao,^{1,*} Liwei Ge,^{1,*} Daochi Zhang,² Xiang Li,¹ Jialin Pan,¹
Yao Wang,¹ Rui-Xue Xu,^{1,3} YiJing Yan,¹ and Xiao Zheng^{2,3,†}

¹*Hefei National Research Center for Physical Sciences at the Microscale, University of Science and Technology of China, Hefei, Anhui 230026, China*

²*Department of Chemistry, Fudan University, Shanghai 200438, China*

³*Hefei National Laboratory, Hefei, Anhui 230088, China*

(Dated: Submitted on June 18, 2025; updated on November 12, 2025)

Reducing computational scaling for simulating non-Markovian dissipative dynamics using artificial neural networks is both a major focus and formidable challenge in open quantum systems. To enable neural quantum states (NQSs), we encode environmental memory in dissipatons (quasi-particles with characteristic lifetimes), yielding the dissipaton-embedded quantum master equation (DQME). The resulting NQS-DQME framework achieves a compact representation of both many-body correlations and non-Markovian memory. Benchmarking against numerically exact hierarchical equations of motion confirms NQS-DQME maintains comparable accuracy while enhancing scalability and interpretability. This methodology opens new paths to explore non-Markovian open quantum dynamics in previously intractable systems.

Introduction. Many-body open quantum systems (OQSs) have attracted wide attention due to their profound applications across diversified fields [1–3]. Accurately characterizing quantum correlations is crucial for the studies of many-body OQSs. For instance, the Kondo correlation between a magnetic molecule (the primary system) and a substrate (the environment) critically determines the electric conductance across the molecule-substrate interface [4–7], exemplifying spatially extended quantum correlations. Similarly, non-Markovian memory effects arising from system-environment coupling [8–10] can lead to complex scaling relations in the dissipative dynamics of OQSs [11, 12], demonstrating temporally persistent quantum correlations [13–16].

Numerically exact approaches [17–30], including the hierarchical equations of motion (HEOM) [31–34], have been developed to simulate non-Markovian open quantum dynamics. However, their applicability remains significantly constrained by the exponential wall inherent to the quantum many-body problem [35], as their computational costs typically scale exponentially with both system size and environmental memory complexity. To address this challenge, tensor network states (TNSs) [36–46] have been utilized to compress the representation of quantum correlations. However, while TNSs successfully reduce the required number of dynamical variables, the resulting approaches still encounter difficulties when area laws are violated [47]. Particularly, TNSs often require large bond dimensions when representing intermediate states during temporal evolution [48, 49] and strong system-environment correlation [42].

Neural quantum states (NQSs) [50], which leverage the power of artificial neural networks, have emerged as a promising method for tackling the exponential wall prob-

lem in many-body OQSs [51–56]. NQSs have demonstrated more expressive power than TNSs [57–59], e.g., in determining the ground states [60, 61] and time evolutions [50] of quantum spin systems. While NQSs have been applied to open quantum systems, simulations have so far been restricted to Markovian environments [62–67]. Consequently, it is believed that addressing non-Markovian memory effects poses the “ultimate toughness test” for simulating open quantum dynamics [68]. Moreover, the sign problem inherent to fermionic environments [21] introduces an additional challenge [69].

A recently developed theory [70] based on the concept of dissipatons (Brownian quasiparticles with complex energies) [71] provides an exact description of non-Markovian open quantum dynamics via the dissipaton-embedded quantum master equation (DQME). In this framework, environmental memory is fully encoded in the dissipatons’ statistical behavior. Formulated with second quantization, the DQME treats system and environmental degrees of freedom on an equal footing [70], making it amenable to a NQS representation of quantum correlations in many-body OQSs.

This Letter aims to establish a framework to integrate the NQS approach with the DQME, and to demonstrate that the unified NQS-DQME approach has the potential to resolve the “ultimate toughness test” of simulating non-Markovian dynamics in strongly correlated OQSs.

Fermionic DQME method. The total Hamiltonian of an OQS comprises three components: $H_T = H_S + H_E + H_{SE}$, where H_S , H_E , and H_{SE} represent the system, environment, and system-environment coupling Hamiltonians, respectively. For a noninteracting fermionic environment linearly coupled to the system, the environmental influence is fully characterized by the hybridization time-correlation function. This function is decomposed into a sum of exponentials, $C^\sigma(t) = \sum_j \eta_j^\sigma e^{-\gamma_j^\sigma t}$, which defines the dissipatons [70–72]. Here, j labels the dissipaton levels, and σ denotes the dissipaton charge ($\sigma = +$ for hole-type; $\sigma = -$ for electron-type). The imaginary

* These authors contributed equally to this work.

† xzheng@fudan.edu.cn

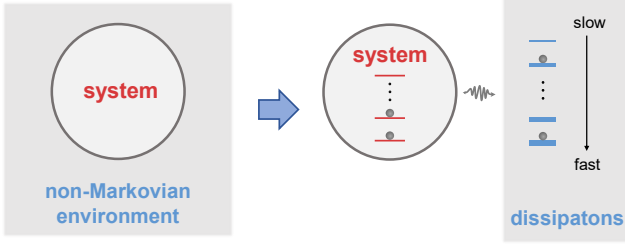


FIG. 1. Schematic of the fermionic DQME theory, mapping the original OQS (left) to a dissipaton-embedded system (right). Red and blue bars represent the N_s system fermion energy levels and N_e memory-carrying dissipaton levels, respectively. Broadening of blue bars indicates each dissipaton's decay rate (inverse lifetime).

and real parts of γ_j^σ correspond to the dissipaton energy and inverse lifetime, respectively, while η_j^σ quantifies the system-dissipaton coupling strength. Crucially, the long-time behavior of $C^\sigma(t)$, and hence the non-Markovian effects, is dominated by the long-lived dissipatons that are strongly coupled to the system.

Figure 1 illustrates the fermionic DQME theory, where the original OQS is mapped to a dissipaton-embedded system described in terms of the reduced density tensor (RDT), $\rho = \rho(\vec{n}, \vec{n}'; \vec{m}^-, \vec{m}^+)$. Here, vectors \vec{n} and \vec{n}' describe system fermion configurations, while \vec{m}^- and \vec{m}^+ represent electron-type and hole-type dissipaton configurations, respectively. The RDT elements with $(\vec{m}^-, \vec{m}^+) = \vec{0}$ yield the system's reduced density operator (RDO). As shown in Fig. 1, each level can accommodate at most one fermion or dissipaton in accordance with the Pauli exclusion principle. In practice, a maximal dissipaton occupation number M_{\max} is introduced to facilitate the numerical solution of the DQME [70].

The fermionic DQME is given by (with $e = \hbar = 1$) [70]:

$$\begin{aligned} \dot{\rho} = \mathcal{L}\rho = & -i[H_s, \rho] - \sum_j \left(\gamma_j^- \hat{N}_j \rho + \gamma_j^+ \rho \hat{N}_j \right) \\ & - i \sum_j \left[(\hat{c}_\nu^\dagger \hat{b}_j \rho - \hat{b}_j \rho \hat{c}_\nu^\dagger) + (\hat{c}_\nu \rho \hat{b}_j^\dagger - \rho \hat{b}_j^\dagger \hat{c}_\nu) \right] \\ & - i \sum_j \left[-\eta_j^- \hat{c}_\nu \hat{b}_j^\dagger \rho - (\eta_j^+)^* \hat{b}_j^\dagger \rho \hat{c}_\nu \right] \\ & - i \sum_j \left[\eta_j^+ \hat{c}_\nu^\dagger \rho \hat{b}_j + (\eta_j^-)^* \rho \hat{b}_j \hat{c}_\nu^\dagger \right]. \end{aligned} \quad (1)$$

Here, \hat{c}_ν^\dagger (\hat{c}_ν) creates (annihilates) a fermion at the ν -th system fermion level, \hat{b}_j^\dagger (\hat{b}_j) creates (annihilates) a dissipaton at j -th level, and $\hat{N}_j = \hat{b}_j^\dagger \hat{b}_j$ gives the dissipaton occupation. The RDO of the system, ρ_0 , is obtained by projecting ρ onto the dissipaton vacuum.

Fundamentally, dissipatons share similarities with previously proposed pseudomodes [17, 18, 73–76], and the DQME is formally equivalent to the exact HEOM theory [33, 34] for reduced system dynamics.

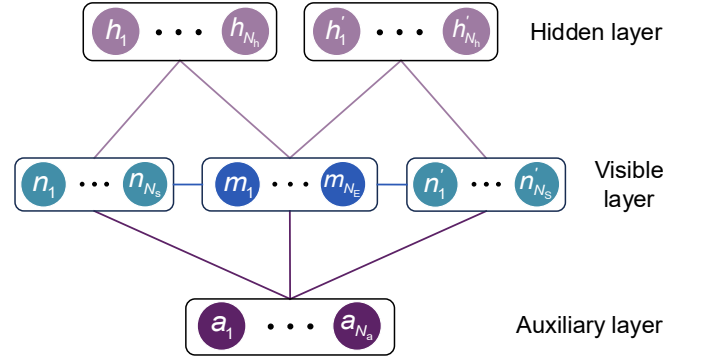


FIG. 2. Structure of the neural network representing $\rho_{\text{pre}}(\vec{n}, \vec{n}'; \vec{m})$. Boxes group nodes of the same type. The visible layer comprises $2N_s + N_e$ nodes, representing elements of \vec{n} , \vec{n}' , and \vec{m} , respectively. Connecting lines between boxes indicate that every node in one box is linked to all nodes in the other box through weighted connections.

NQS representation of RDT. We now establish a NQS framework to characterize quantum correlations in OQSs. This framework begins by constructing a preliminary RDT as

$$\rho_{\text{pre}}(\vec{n}, \vec{n}'; \vec{m}) = \sum_{\{\vec{a}\}} \psi(\vec{n}; \vec{m}; \vec{a}) \varphi^*(\vec{n}'; \vec{m}; \vec{a}), \quad (2)$$

where $\vec{m} \equiv (\vec{m}^-, \vec{m}^+)$. The wavefunctions ψ and φ are expressed using restricted Boltzmann machines (RBMs) [50, 62–64, 66], with \vec{a} denoting N_a auxiliary nodes of binary values. This construction faithfully captures the mapping illustrated in Fig. 1: the dissipaton states \vec{m} encode the non-Markovian memory of the environment, while \vec{a} accounts for the Markovian background responsible for the finite lifetimes of the dissipatons. Furthermore, this architecture inherently helps preserve the hermiticity and positive definiteness of the resulting RDO.

Specifically,

$$\psi(\vec{n}; \vec{m}; \vec{a}) = \sum_{\{\vec{h}\}} \exp[-E_{\vec{h}}(\vec{n}; \vec{m}; \vec{a})], \quad (3)$$

where \vec{h} represents N_h hidden nodes, and

$$\begin{aligned} E_{\vec{h}}(\vec{n}; \vec{m}; \vec{a}) = & \mathbf{a}^T \mathbf{b} + \mathbf{n}^T \mathbf{c} + \mathbf{m}^T \mathbf{d} + \mathbf{h}^T \mathbf{g} + \mathbf{n}^T \mathbf{D} \mathbf{m} \\ & + \mathbf{m}^T \mathbf{K} \mathbf{a} + \mathbf{n}^T \mathbf{X} \mathbf{h} + \mathbf{n}^T \mathbf{X}' \mathbf{a} + \mathbf{m}^T \mathbf{Y} \mathbf{h}. \end{aligned} \quad (4)$$

Here, $(\mathbf{b}, \mathbf{c}, \mathbf{d}, \mathbf{g})$ denote complex-valued bias vectors, while $(\mathbf{D}, \mathbf{K}, \mathbf{X}, \mathbf{X}', \mathbf{Y})$ represent complex-valued weight matrices of the RBM. An analogous RBM structure describes $\varphi(\vec{n}'; \vec{m}; \vec{a})$.

Figure 2 depicts the neural network architecture for $\rho_{\text{pre}}(\vec{n}, \vec{n}'; \vec{m})$. The complete analytic expression is provided in the Supplemental Material (SM) [77]. The dissipaton-related nodes in the visible layer explicitly encode the environmental memory content, in distinct contrast to conventional RBMs used to represent OQSs coupled to memoryless environments [62–64].

The dimensionality of RDT can be reduced by leveraging its inherent symmetry and sparsity [78]. First, we enforce the symmetry constraint by constructing

$$\rho_{\text{sym}}(\vec{s}) = \rho_{\text{pre}}(\vec{s}) + (-1)^{\lfloor M^-/2 \rfloor + \lfloor M^+/2 \rfloor} \rho_{\text{pre}}^*(\vec{s}^T), \quad (5)$$

where $\lfloor \cdot \rfloor$ denotes the floor function, $M^\sigma = \sum_j m_j^\sigma$, and m_j^σ is the j -th element of \vec{m}^σ . Here, $\vec{s} \equiv (\vec{n}, \vec{n}'; \vec{m}^-, \vec{m}^+)$ represents a visible state, while $\vec{s}^T \equiv (\vec{n}', \vec{n}; \vec{m}^+, \vec{m}^-)$ is its block-swapped counterpart. Next, we introduce a filter function $f_{\text{spa}}(\vec{s})$ that identifies, *a priori*, the zero elements of ρ based on the sparsity pattern dictated by the forms of H_S and H_{SE} [79]. In practice, $f_{\text{spa}}(\vec{s})$ normally reduces the \vec{s} -space by over an order of magnitude [77]. The resulting symmetrized and filtered RDT is given by $\rho(\vec{s}) = f_{\text{spa}}(\vec{s})\rho_{\text{sym}}(\vec{s})$.

Within the RBM representation, the RDT is expressed parametrically as ρ_α , where α denotes the complete set of RBM parameters. The total number of parameters is approximately $N_{\text{para}} \approx 2N_S(N_h + N_a) + N_E(4N_h + N_a)$. Provided that N_h and N_a scale linearly with $2N_S + N_E$, N_{para} scales approximately quadratically with the dimension of the dissipaton-embedded system [77]. This scaling is vastly more favorable than that of the original DQME, where the RDT dimension grows as $N_{\text{RDT}} \approx 4^{N_S} N_E^{M_{\text{max}}}$.

Time evolution of NQS-DQME. Within the NQS framework, the exact DQME of Eq. (1) is projected onto the parameter space. Through the time-dependent variational principle [63, 80], the problem is transformed into determining the time evolution of the parameters $\alpha(t)$. Numerically, this is achieved by minimizing the 2-norm $\Delta s^2 = \|\dot{\rho}_\alpha - \mathcal{L}\rho_\alpha\|_2^2$, which yields a linear equation for $\dot{\alpha}$ at each time step:

$$\mathcal{S}\dot{\alpha} = \mathcal{F}. \quad (6)$$

Here, \mathcal{S} and \mathcal{F} are a matrix and a vector defined in the parameter space, respectively. Evaluating their elements requires summing over all visible states \vec{s} , which we perform using the Markov chain Monte Carlo algorithm [81]. The sampling process employs the Metropolis-Hastings criterion [82] with a customized probability distribution $p(\vec{s}) \propto e^{-3(M^+ + M^-)}$. The derivatives $\dot{\alpha}$ are then obtained by solving Eq. (6) [83], and $\alpha(t)$ are updated using the fourth-order Runge-Kutta algorithm [84, 85]. Further details are provided in the SM [77].

To demonstrate the practicality and accuracy of the NQS-DQME approach, we investigate non-Markovian dynamics in two strongly correlated OQSs. We employ the numerically exact fermionic HEOM method implemented in the HEOM-QUICK2 program [86] as the benchmark to provide reference values.

Case 1: non-Markovian charge relaxation with emergent Kondo correlations. We consider an OQS comprising a localized impurity symmetrically coupled to two noninteracting electron reservoirs. This setup is important for understanding electron transport through

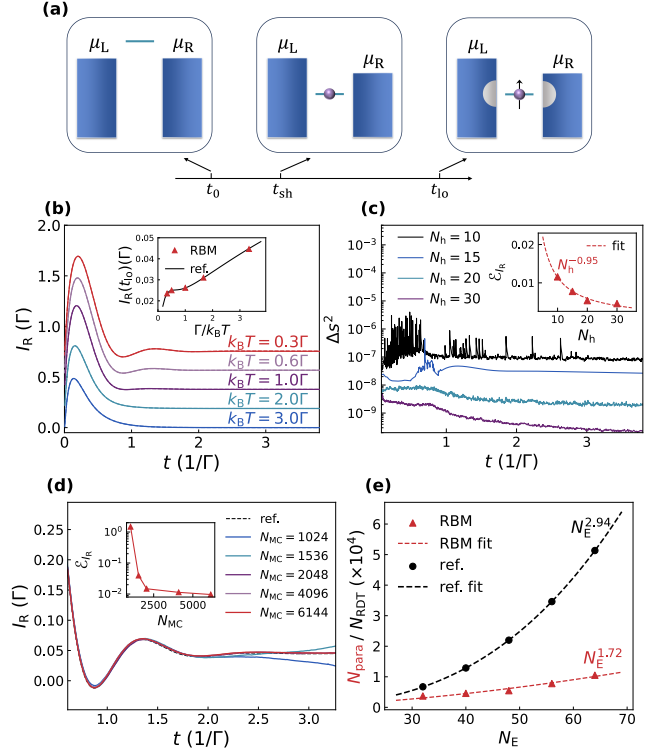


FIG. 3. (a) Schematic of open quantum dynamics for an impurity coupled to left (L) and right (R) reservoirs with chemical potentials μ_L and μ_R . Gray shaded regions in the reservoirs represent Kondo clouds screening the impurity's localized spin. (b) $I_R(t)$ at different temperatures. The NQS-DQME results (solid lines, vertically offset for clarity) are benchmarked against HEOM reference values. Inset: steady-state current versus inverse temperature. (c) Time evolution of Δs^2 for $k_B T = 0.3\Gamma$, computed with different $N_h = N_a$. Inset: \mathcal{E}_{IR} versus N_h with a power function fit. (d) $I_R(t)$ at $k_B T = 0.3\Gamma$ computed with different N_{MC} . Inset: \mathcal{E}_{IR} versus N_{MC} . (e) Number of dynamical variables explicitly accessed in the NQS-DQME and HEOM methods versus N_E , where N_E increases monotonically as T decreases. Dashed lines are power function fits to the scattered data with $M_{\text{max}} = 3$. System parameters (in units of Γ): $\epsilon_0 = U_0/2 = 2$, $\Delta\epsilon = -7$, and $\Delta U = 6$; see the SM for further details [77].

molecular junctions. The OQS is described by the single-impurity Anderson model [87]. The impurity Hamiltonian is $H_S(t) = \epsilon_0(\hat{n}_\uparrow + \hat{n}_\downarrow) + U_0\hat{n}_\uparrow\hat{n}_\downarrow + \Theta(t - t_0)[\Delta\epsilon(\hat{n}_\uparrow + \hat{n}_\downarrow) + \Delta U\hat{n}_\uparrow\hat{n}_\downarrow]$, where \hat{n}_s is the occupation operator for spin- s electrons, ϵ_0 is the impurity energy, and U_0 is the Coulomb interaction energy. At time $t_0 = 0$, a sudden quench shifts the impurity's parameters by $\Delta\epsilon$ and ΔU , and a bias voltage is applied, establishing a chemical potential difference between the reservoirs. Figure 3(a) depicts the ensuing open quantum dynamics. The impurity level shift triggers electron transfer from the reservoirs to the impurity on a relatively short timescale. Subsequently, reservoir electrons redistribute their spins to screen the impurity's localized spin, leading to the forma-

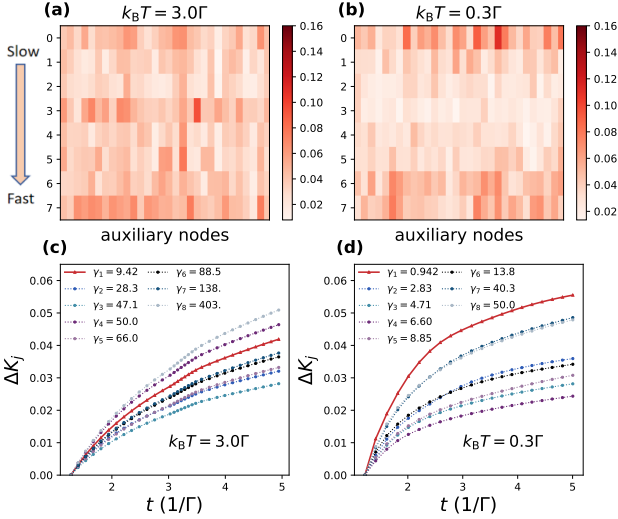


FIG. 4. Visualization of the RBM parameters for the open quantum dynamics shown in Fig. 3. (a,b) Heatmaps of $|\mathbf{K}(t_{10}) - \mathbf{K}(t_{sh})|$ at (a) $k_B T = 3.0\Gamma$ and (b) $k_B T = 0.3\Gamma$, for $t_{sh} = 1.25/\Gamma$ and $t_{10} = 5/\Gamma$. The vertical axis indexes dissipaton levels (with decay rates sorted from slowest to fastest), and the horizontal axis indexes the auxiliary nodes. (c,d) Time evolution of the auxiliary-layer-averaged weight difference for the j th dissipaton level, $\Delta K_j = |K_j(t) - K_j(t_{sh})|$, at (c) $k_B T = 3.0\Gamma$ and (d) $k_B T = 0.3\Gamma$. Here, $\gamma_j \equiv \text{Re}(\gamma_j^\sigma)$ denotes the decay rate in unit of $1/\Gamma$. The red line tracks the slowest-decaying dissipaton level.

tion of Kondo states at the impurity-reservoir interfaces over a longer timescale [11, 12, 88]. We denote t_{sh} and t_{10} as representative times for the short-time and long-time regions, respectively.

Figure 3(b) shows the time-dependent current $I_R(t)$ at various temperatures. At low temperatures, $I_R(t)$ exhibits pronounced oscillations near $t = 1/\Gamma$, where Γ is the impurity-reservoir hybridization strength. These transient oscillations are a characteristic signature of non-Markovian memory, arising from coherent impurity-reservoir coupling under suppressed thermal fluctuations. The same coupling enhances Kondo correlations, leading to the increase in the steady-state current (evaluated at t_{10}) as temperature decreases, as seen in the inset.

Within the NQS-DQME framework, the expectation value of an observable \hat{X} , $X = \langle \hat{X} \rangle$, is evaluated from ρ_α [77]. The accuracy of the results is quantified by the relative error:

$$\mathcal{E}_X \equiv \frac{\int_{t_0}^{t_{10}} |X(t) - X^{\text{ref}}(t)| dt}{\int_{t_0}^{t_{10}} \frac{1}{2} (|X(t)| + |X^{\text{ref}}(t)|) dt}. \quad (7)$$

As shown in Fig. 3(b), the NQS-DQME results exhibit excellent agreement with the reference data, with $\mathcal{E}_{I_R} < 1\%$ across the entire temperature range.

To explore the tradeoff between numerical cost and accuracy, we examine the low temperature regime ($k_B T =$

0.3Γ), where non-Markovian effects are prominent. The dissipaton-embedded system comprises 2 system levels coupled inhomogeneously to 64 dissipaton levels. Figure 3(c) shows the evolution of the precision metric Δs^2 for different numbers of hidden nodes N_h . The magnitude of Δs^2 decreases by orders of magnitude with a linear increase in N_h , demonstrating rapid convergence. Similarly, Fig. 3(d) shows that accurate results are achieved with relatively few Monte Carlo samples (N_{MC}). Furthermore, Fig. 3(e) demonstrates that the NQS-DQME approach achieves high accuracy ($\Delta s^2 < 10^{-8}$) while utilizing drastically fewer dynamical variables than the conventional HEOM method. This comparison is conducted under equivalent conditions, as the same symmetry and sparsity relations are incorporated into both methods. These results collectively highlight the outstanding expressive power of the RBM for characterizing non-Markovian open quantum dynamics.

An important hypothesis in open quantum dynamics is that non-Markovian memory is crucial for long-time phenomena like the formation of Kondo-correlated states. However, directly verifying this by tracking dynamical variables in conventional methods such as the HEOM or the original DQME is prohibitively difficult due to their high dimensionality. In contrast, the NQS-DQME framework makes such tracking feasible, since the RDT is represented by weight matrices that form a much lower-dimensional parameter space.

This capability is demonstrated in Fig. 4, which visualizes the evolution of the RBM weight matrix \mathbf{K} connecting dissipaton-level nodes to auxiliary nodes for the open quantum dynamics shown in Fig. 3. A comparison of the heatmaps in Fig. 4(a) and (b) shows that the weight changes, $|\mathbf{K}(t_{10}) - \mathbf{K}(t_{sh})|$, are significantly more pronounced for the slowest-decaying dissipaton level at the lower temperature. This is indicated by the darker top row in Fig. 4(b). This observation is further confirmed by the time evolution of the auxiliary-layer-averaged weight difference $\Delta K_j(t)$ in Fig. 4(c) and (d), where the slowest-decaying dissipaton level (red line) becomes increasingly prominent as temperature decreases, directly linking the non-Markovian memory to the emerging Kondo effect.

Case 2: non-Markovian spin relaxation with intertwined Kondo correlations. We now examine a more complex OQS comprising two impurities coupled to a reservoir. This setup directly models recent experimental studies of coherent spin dynamics in surface molecules [14, 15]. The system Hamiltonian is $H_s(t) = \sum_{\nu=1,2} [\epsilon_\nu (\hat{n}_{\nu\uparrow} + \hat{n}_{\nu\downarrow}) + U_0 \hat{n}_{\nu\uparrow} \hat{n}_{\nu\downarrow}] - \Theta(t - t_0) J \hat{\mathbf{S}}_1 \cdot \hat{\mathbf{S}}_2$, where the final term activates a ferromagnetic exchange interaction ($J > 0$) between the impurities at time t_0 .

Figure 5(a) shows the relaxation dynamics following the sudden activation of the exchange interaction. The initially independent localized spins on the two impurities gradually evolve towards parallel alignment. This results in a localized high-spin state that cannot be fully screened by the reservoir electrons. This underscreening progressively suppresses Kondo correlations during the

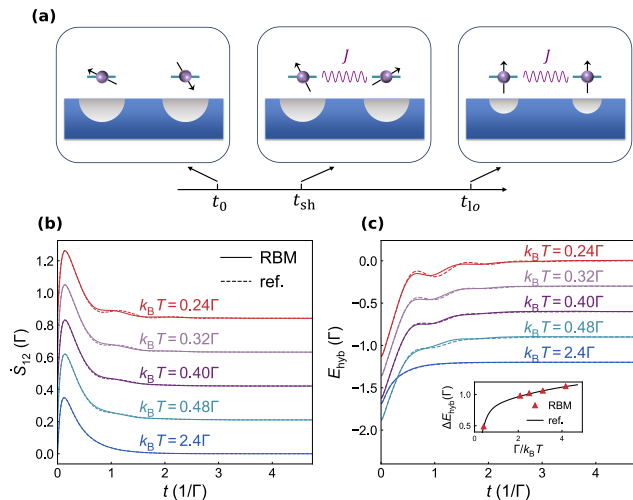


FIG. 5. (a) Schematic of quantum dissipative dynamics for two impurities coupled to a reservoir. Spin-exchange interaction (wavy line) and Kondo clouds (gray regions) are shown, where cloud extents indicate Kondo correlation strengths. Time evolution of (b) \dot{S}_{12} and (c) E_{hyb} at various temperatures. NQS-DQME results (solid lines, vertically offset for clarity) are benchmarked against HEOM reference values. Inset in (c): $\Delta E_{hyb} = E_{hyb}(t_{lo}) - E_{hyb}(t_0)$ versus inverse temperature. The increase in ΔE_{hyb} with decreasing temperature indicates weakened Kondo correlations in the long-time limit. System parameters (in units of Γ): $\epsilon_0 = -U_0/2 = -6$, and $J = 8$; see the SM for details [77].

temporal evolution [7, 89, 90].

Figure 5(b) and (c) depict the time derivative of the inter-impurity spin correlation, $\dot{S}_{12} = \frac{\partial}{\partial t} \langle \hat{S}_1 \cdot \hat{S}_2 \rangle$, and the impurity-reservoir hybridization energy, $E_{hyb} = \langle H_{SE} \rangle$, respectively, at various temperatures. We plot \dot{S}_{12} rather than S_{12} to highlight its more pronounced oscillatory behavior. At low temperatures, both quantities exhibit strong oscillations, a hallmark of non-Markovian mem-

ory effects.

The NQS-DQME results are in excellent agreement with the reference values, with maximum errors $\mathcal{E}_{S_{12}}$ and $\mathcal{E}_{E_{hyb}}$ both below 1% for $t_{lo} > 3/\Gamma$. This quantitative agreement is remarkable, as the spin relaxation dynamics are governed by the complex interplay of direct impurity correlations and impurity-reservoir Kondo correlations. Furthermore, similar to Case 1, the NQS representation achieves this accuracy with a significantly reduced number of dynamical variables compared to conventional approaches [77].

Summary. We have developed a NQS framework for the efficient simulation of non-Markovian open quantum dynamics by integrating the dissipaton concept into the ansatz. This NQS-DQME approach provides a compact and physically interpretable representation of the RDT, enabling the simultaneous treatment of complex environmental memory and many-body correlations with significantly enhanced computational efficiency.

While the current framework shares a common challenge with many NQS methods, i.e., the computationally demanding minimization of the loss function Δs^2 [64]. This bottleneck can be addressed using advanced optimizers and more sophisticated network architectures. Given its proven scalability and interpretability, the NQS-DQME approach presents a promising and versatile platform for exploring rich quantum phenomena in correlated, non-Markovian settings.

ACKNOWLEDGMENTS

Support from the National Natural Science Foundation of China (Grants No. 22393912, No. 22321003, No. 22103073, No. 22173088, and No. 22373091), the Innovation Program for Quantum Science and Technology (Grants No. 2021ZD0303301 and No. 2021ZD0303306), the AI for Science Foundation of Fudan University (Grant No. FudanX24AI023), and the Strategic Priority Research Program of Chinese Academy of Sciences (Grant No. XDB0450101) is gratefully acknowledged.

[1] G. S. Engel, T. R. Calhoun, E. L. Read, T. Ahn, T. Mančal, Y. Cheng, R. E. Blankenship, and G. R. Fleming, “Evidence for wavelike energy transfer through quantum coherence in photosynthetic systems,” *Nature* **446**, 782 (2007).
 [2] R. Hildner, D. Brinks, J. B. Nieder, R. J. Cogdell, and N. F. van Hulst, “Quantum Coherent Energy Transfer over Varying Pathways in Single Light-Harvesting Complexes,” *Science* **340**, 1448 (2013).
 [3] I. Piquero-Zulaica, J. Lobo-Checa, Z. M. A. El-Fattah, J. E. Ortega, F. Klappenberger, W. Auwärter, and J. V. Barth, “Engineering quantum states and electronic landscapes through surface molecular nanoarchitectures,” *Rev. Mod. Phys.* **94**, 045008 (2022).
 [4] K. G. Wilson, “The renormalization group: Critical phe-

nomena and the Kondo problem,” *Rev. Mod. Phys.* **47**, 773 (1975).
 [5] V. Madhavan, W. Chen, T. Jamneala, M. F. Crommie, and N. S. Wingreen, “Tunneling into a Single Magnetic Atom: Spectroscopic Evidence of the Kondo Resonance,” *Science* **280**, 567 (1998).
 [6] A. Zhao, Q. Li, L. Chen, H. Xiang, W. Wang, S. Pan, B. Wang, X. Xiao, J. Yang, J. G. Hou, and Q. Zhu, “Controlling the Kondo Effect of an Adsorbed Magnetic Ion Through Its Chemical Bonding,” *Science* **309**, 1542 (2005).
 [7] X. Li et al., “Molecular molds for regularizing Kondo states at atom/metal interfaces,” *Nat. Commun.* **11**, 2566 (2020).
 [8] H. P. Breuer, E. M. Laine, J. Piilo, and B. Vacchini,

- “Colloquium: Non-Markovian dynamics in open quantum systems,” *Rev. Mod. Phys.* **88**, 021002 (2016).
- [9] I. De Vega and D. Alonso, “Dynamics of non-Markovian open quantum systems,” *Rev. Mod. Phys.* **89**, 015001 (2017).
- [10] B. Debecker, J. Martin, and F. m. c. Damanet, “Controlling Matter Phases beyond Markov,” *Phys. Rev. Lett.* **133**, 140403 (2024).
- [11] F. B. Anders and A. Schiller, “Real-time dynamics in quantum-impurity systems: A time-dependent numerical renormalization-group approach,” *Phys. Rev. Lett.* **95**, 196801 (2005).
- [12] X. Ding, D. Zhang, H.-D. Zhang, X. Zheng, and Y. Yan, “Unveiling hidden scaling relations in dissipative relaxation dynamics of strongly correlated quantum impurity systems,” *J. Chem. Phys.* **161**, 174120 (2024).
- [13] X. Zheng, Y. Yan, and M. Di Ventura, “Kondo Memory in Driven Strongly Correlated Quantum Dots,” *Phys. Rev. Lett.* **111**, 086601 (2013).
- [14] K. Yang, W. Paul, S. H. Phark, P. Willke, Y. Bae, T. Choi, T. Esat, A. Ardavan, A. J. Heinrich, and C. P. Lutz, “Coherent spin manipulation of individual atoms on a surface,” *Science* **366**, 509 (2019).
- [15] L. M. Veldman, L. Farinacci, R. Rejali, R. Broekhoven, J. Gobeil, D. Coffey, M. Ternes, and A. F. Otte, “Free coherent evolution of a coupled atomic spin system initialized by electron scattering,” *Science* **372**, 964 (2021).
- [16] X. Ding, J. Cao, X. Zheng, and L. Ye, “Tracking spin flip-flop dynamics of surface molecules with quantum dissipation theory,” *J. Chem. Phys.* **162**, 084114 (2025).
- [17] D. Tamascelli, A. Smirne, S. F. Huelga, and M. B. Plenio, “Nonperturbative treatment of non-Markovian dynamics of open quantum systems,” *Phys. Rev. Lett.* **120**, 030402 (2018).
- [18] N. Lambert, S. Ahmed, M. Cirio, and F. Nori, “Modelling the ultra-strongly coupled spin-boson model with unphysical modes,” *Nat. Commun.* **10**, 3721 (2019).
- [19] W. T. Strunz, L. Diósi, and N. Gisin, “Open System Dynamics with Non-Markovian Quantum Trajectories,” *Phys. Rev. Lett.* **82**, 1801 (1999).
- [20] J. Shao, “Decoupling quantum dissipation interaction via stochastic fields,” *J. Chem. Phys.* **120**, 5053 (2004).
- [21] L. Han, V. Chernyak, Y. Yan, X. Zheng, and Y. Yan, “Stochastic Representation of Non-Markovian Fermionic Quantum Dissipation,” *Phys. Rev. Lett.* **123**, 050601 (2019).
- [22] J. T. Stockburger and H. Grabert, “Exact c -Number Representation of Non-Markovian Quantum Dissipation,” *Phys. Rev. Lett.* **88**, 170407 (2002).
- [23] D. Suess, A. Eisfeld, and W. T. Strunz, “Hierarchy of stochastic pure states for open quantum system dynamics,” *Phys. Rev. Lett.* **113**, 150403 (2014).
- [24] G. Cohen, E. Gull, D. R. Reichman, and A. J. Millis, “Taming the Dynamical Sign Problem in Real-Time Evolution of Quantum Many-Body Problems,” *Phys. Rev. Lett.* **115**, 266802 (2015).
- [25] A. Erpenbeck, E. Gull, and G. Cohen, “Quantum Monte Carlo Method in the Steady State,” *Phys. Rev. Lett.* **130**, 186301 (2023).
- [26] F. Güttge, F. B. Anders, U. Schollwöck, E. Eidelstein, and A. Schiller, “Hybrid NRG-DMRG approach to real-time dynamics of quantum impurity systems,” *Phys. Rev. B* **87**, 115115 (2013).
- [27] M. A. Cazalilla and J. B. Marston, “Time-Dependent Density-Matrix Renormalization Group: A Systematic Method for the Study of Quantum Many-Body Out-of-Equilibrium Systems,” *Phys. Rev. Lett.* **88**, 256403 (2002).
- [28] A. U. J. Lode, C. Lévêque, L. B. Madsen, A. I. Streltsov, and O. E. Alon, “Colloquium: Multiconfigurational time-dependent Hartree approaches for indistinguishable particles,” *Rev. Mod. Phys.* **92**, 011001 (2020).
- [29] H. Wang and M. Thoss, “Numerically exact quantum dynamics for indistinguishable particles: The multilayer multiconfiguration time-dependent Hartree theory in second quantization representation,” *J. Chem. Phys.* **131**, 024114 (2009).
- [30] H. Weimer, A. Kshetrimayum, and R. Orús, “Simulation methods for open quantum many-body systems,” *Rev. Mod. Phys.* **93**, 015008 (2021).
- [31] Y. Tanimura and R. Kubo, “Time evolution of a quantum system in contact with a nearly Gaussian-Markovian noise bath,” *J. Phys. Soc. Jpn.* **58**, 101 (1989).
- [32] Y. an Yan, F. Yang, Y. Liu, and J. Shao, “Hierarchical approach based on stochastic decoupling to dissipative systems,” *Chem. Phys. Lett.* **395**, 216 (2004).
- [33] J. Jin, X. Zheng, and Y. Yan, “Exact dynamics of dissipative electronic systems and quantum transport: Hierarchical equations of motion approach,” *J. Chem. Phys.* **128**, 234703 (2008).
- [34] Z. Li, N. Tong, X. Zheng, D. Hou, J. Wei, J. Hu, and Y. Yan, “Hierarchical Liouville-Space Approach for Accurate and Universal Characterization of Quantum Impurity Systems,” *Phys. Rev. Lett.* **109**, 266403 (2012).
- [35] W. Kohn, “Nobel Lecture: Electronic structure of matter—wave functions and density functionals,” *Rev. Mod. Phys.* **71**, 1253 (1999).
- [36] A. Klümper, A. Schadschneider, and J. Zittartz, “Matrix Product Ground States for One-Dimensional Spin-1 Quantum Antiferromagnets,” *Europhys. Lett.* **24**, 293 (1993).
- [37] S. Flannigan, F. Damanet, and A. J. Daley, “Many-body quantum state diffusion for non-Markovian dynamics in strongly interacting systems,” *Phys. Rev. Lett.* **128**, 063601 (2022).
- [38] D. Jaschke, S. Montangero, and L. D. Carr, “One-dimensional many-body entangled open quantum systems with tensor network methods,” *Quantum Sci. Technol.* **4**, 013001 (2018).
- [39] V. Link, H.-H. Tu, and W. T. Strunz, “Open quantum system dynamics from infinite tensor network contraction,” *Phys. Rev. Lett.* **132**, 200403 (2024).
- [40] A. H. Werner, D. Jaschke, P. Silvi, M. Kliesch, T. Calarco, J. Eisert, and S. Montangero, “Positive tensor network approach for simulating open quantum many-body systems,” *Phys. Rev. Lett.* **116**, 237201 (2016).
- [41] A. Strathearn, P. Kirton, D. Kilda, J. Keeling, and B. W. Lovett, “Efficient non-Markovian quantum dynamics using time-evolving matrix product operators,” *Nat. Commun.* **9**, 3322 (2018).
- [42] Q. Shi, Y. Xu, Y. Yan, and M. Xu, “Efficient propagation of the hierarchical equations of motion using the matrix product state method,” *J. Chem. Phys.* **148**, 174102 (2018).
- [43] Y. Ke, R. Borrelli, and M. Thoss, “Hierarchical equations of motion approach to hybrid fermionic and bosonic environments: Matrix product state formulation in twin

- space,” *J. Chem. Phys.* **156**, 194102 (2022).
- [44] F. Schwarz, I. Weymann, J. von Delft, and A. Weichselbaum, “Nonequilibrium steady-state transport in quantum impurity models: A thermofield and quantum quench approach using matrix product states,” *Phys. Rev. Lett.* **121**, 137702 (2018).
- [45] M. R. Jørgensen and F. A. Pollock, “Exploiting the Causal Tensor Network Structure of Quantum Processes to Efficiently Simulate Non-Markovian Path Integrals,” *Phys. Rev. Lett.* **123**, 240602 (2019).
- [46] Y. Zhao, “The hierarchy of Davydov’s Ansatz: From guesswork to numerically “exact” many-body wave functions,” *J. Chem. Phys.* **158**, 080901 (2023).
- [47] J. Eisert, M. Cramer, and M. B. Plenio, “Colloquium: Area laws for the entanglement entropy,” *Rev. Mod. Phys.* **82**, 277 (2010).
- [48] L. Bonnes, D. Charrier, and A. M. Läuchli, “Dynamical and steady-state properties of a Bose-Hubbard chain with bond dissipation: A study based on matrix product operators,” *Phys. Rev. A* **90**, 033612 (2014).
- [49] H. Weimer, A. Kshetrimayum, and R. Orús, “Simulation methods for open quantum many-body systems,” *Rev. Mod. Phys.* **93**, 015008 (2021).
- [50] G. Carleo and M. Troyer, “Solving the quantum many-body problem with artificial neural networks,” *Science* **355**, 602 (2017).
- [51] J. Hermann, J. Spencer, K. Choo, A. Mezzacapo, W. M. C. Foulkes, D. Pfau, G. Carleo, and F. Noé, “Ab initio quantum chemistry with neural-network wavefunctions,” *Nat. Rev. Chem.* **7**, 692 (2023).
- [52] O. Sharir, Y. Levine, N. Wies, G. Carleo, and A. Shashua, “Deep autoregressive models for the efficient variational simulation of many-body quantum systems,” *Phys. Rev. Lett.* **124**, 020503 (2020).
- [53] H. Shang, C. Guo, Y. Wu, Z. Li, and J. Yang, “Solving Schrödinger Equation with a Language Model,” arXiv preprint arXiv:2307.09343 (2023).
- [54] G. Torlai and R. G. Melko, “Latent Space Purification via Neural Density Operators,” *Phys. Rev. Lett.* **120**, 240503 (2018).
- [55] K. Donatella, Z. Denis, A. Le Boité, and C. Ciuti, “Dynamics with autoregressive neural quantum states: Application to critical quench dynamics,” *Phys. Rev. A* **108**, 022210 (2023).
- [56] L. Ye, Y. Wang, and X. Zheng, “Simulating many-body open quantum systems by harnessing the power of artificial intelligence and quantum computing,” *J. Chem. Phys.* **162**, 120901 (2025).
- [57] J. Chen, S. Cheng, H. Xie, L. Wang, and T. Xiang, “Equivalence of restricted Boltzmann machines and tensor network states,” *Phys. Rev. B* **97**, 085104 (2018).
- [58] O. Sharir, A. Shashua, and G. Carleo, “Neural tensor contractions and the expressive power of deep neural quantum states,” *Phys. Rev. B* **106**, 205136 (2022).
- [59] H. Lange, A. Van de Walle, A. Abedinnia, and A. Bohrdt, “From architectures to applications: A review of neural quantum states,” *Quantum Sci. Technol.* **9**, 040501 (2024).
- [60] D. Wu, R. Rossi, F. Vicentini, and G. Carleo, “From tensor-network quantum states to tensorial recurrent neural networks,” *Phys. Rev. Res.* **5**, L032001 (2023).
- [61] D.-L. Deng, X. Li, and S. Das Sarma, “Quantum entanglement in neural network states,” *Phys. Rev. X* **7**, 021021 (2017).
- [62] A. Nagy and V. Savona, “Variational Quantum Monte Carlo Method with a Neural-Network Ansatz for Open Quantum Systems,” *Phys. Rev. Lett.* **122**, 250501 (2019).
- [63] M. J. Hartmann and G. Carleo, “Neural-Network Approach to Dissipative Quantum Many-Body Dynamics,” *Phys. Rev. Lett.* **122**, 250502 (2019).
- [64] F. Vicentini, A. Biella, N. Regnault, and C. Ciuti, “Variational Neural-Network Ansatz for Steady States in Open Quantum Systems,” *Phys. Rev. Lett.* **122**, 250503 (2019).
- [65] J. Mellak, E. Arrigoni, T. Pock, and W. Von Der Linden, “Quantum transport in open spin chains using neural-network quantum states,” *Phys. Rev. B* **107**, 205102 (2023).
- [66] N. Yoshioka and R. Hamazaki, “Constructing neural stationary states for open quantum many-body systems,” *Phys. Rev. B* **99**, 214306 (2019).
- [67] J. Mellak, E. Arrigoni, and W. von der Linden, “Deep neural networks as variational solutions for correlated open quantum systems,” *Commun. Phys.* **7**, 268 (2024).
- [68] M. Schuld, I. Sinayskiy, and F. Petruccione, “Neural Networks Take on Open Quantum Systems,” *Physics* **12**, 74 (2019).
- [69] G. Carleo, I. Cirac, K. Cranmer, L. Daudet, M. Schuld, N. Tishby, L. Vogt-Maranto, and L. Zdeborová, “Machine learning and the physical sciences,” *Rev. Mod. Phys.* **91**, 045002 (2019).
- [70] X. Li, S. Lyu, Y. Wang, R. Xu, X. Zheng, and Y. Yan, “Toward quantum simulation of non-Markovian open quantum dynamics: A universal and compact theory,” *Phys. Rev. A* **110**, 032620 (2024).
- [71] Y. Yan, “Theory of open quantum systems with bath of electrons and phonons and spins: Many-dissipaton density matrixes approach,” *J. Chem. Phys.* **140**, 054105 (2014).
- [72] J. Hu, R.-X. Xu, and Y. Yan, “Communication: Padé spectrum decomposition of Fermi function and Bose function,” *J. Chem. Phys.* **133**, 101106 (2010).
- [73] B. M. Garraway, “Nonperturbative decay of an atomic system in a cavity,” *Phys. Rev. A* **55**, 2290 (1997).
- [74] M. Cirio, N. Lambert, P. Liang, P. Kuo, Y. Chen, P. Menczel, K. Funo, and F. Nori, “Pseudofermion method for the exact description of fermionic environments: From single-molecule electronics to the Kondo resonance,” *Phys. Rev. Res.* **5**, 033011 (2023).
- [75] J.-D. Lin, P.-C. Kuo, N. Lambert, A. Miranowicz, F. Nori, and Y.-N. Chen, “Non-Markovian quantum exceptional points,” *Nat. Commun.* **16**, 1289 (2025).
- [76] G. Pleasance, B. M. Garraway, and F. Petruccione, “Generalized theory of pseudomodes for exact descriptions of non-Markovian quantum processes,” *Phys. Rev. Res.* **2**, 043058 (2020).
- [77] See Supplemental Material at xxx for more details about the NQS-DQME approach, RBM representation of RDT, and numerical calculations.
- [78] D. Hou, S. Wang, R. Wang, L. Ye, R. Xu, X. Zheng, and Y. Yan, “Improving the efficiency of hierarchical equations of motion approach and application to coherent dynamics in Aharonov–Bohm interferometers,” *J. Chem. Phys.* **142**, 104112 (2015).
- [79] D. Hou, S. K. Wang, R. L. Wang, L. Z. Ye, R. X. Xu, X. Zheng, and Y. J. Yan, “Improving the efficiency of hierarchical equations of motion approach and applica-

- tion to coherent dynamics in Aharonov-Bohm interferometers,” *J. Chem. Phys.* **142**, 104112 (2015).
- [80] M. Reh, M. Schmitt, and M. Gärttner, “Time-dependent variational principle for open quantum systems with artificial neural networks,” *Phys. Rev. Lett.* **127**, 230501 (2021).
- [81] C. J. Geyer, “Practical Markov Chain Monte Carlo,” *Stat. Sci.* **7**, 473 (1992).
- [82] N. Metropolis, A. W. Rosenbluth, M. N. Rosenbluth, A. H. Teller, and E. Teller, “Equation of state calculations by fast computing machines,” *J. Chem. Phys.* **21**, 1087 (1953).
- [83] S.-C. T. Choi, C. C. Paige, and M. A. Saunders, “MINRES-QLP: A Krylov subspace method for indefinite or singular symmetric systems,” *SIAM J. Sci. Comput.* **33**, 1810 (2011).
- [84] W. H. Press, S. A. Teukolsky, W. T. Vetterling, and B. P. Flannery, *Numerical Recipes: The Art of Scientific Computing*, Cambridge University Press, 3 edition, 2007.
- [85] L. Cao, L. Ge, and X. Zheng, RBM-DQME (GitHub Repository), <https://github.com/dumbimm/RBM-DQME/tree/master> (2024).
- [86] D. Zhang, L. Ye, J. Cao, Y. Wang, R.-X. Xu, X. Zheng, and Y. Yan, “HEOM-QUICK2: A general-purpose simulator for fermionic many-body open quantum systems—An update,” *WIREs Comput. Mol. Sci.* **14**, e1727 (2024).
- [87] P. W. Anderson, “Localized Magnetic States in Metals,” *Phys. Rev.* **124**, 41 (1961).
- [88] H. T. M. Nghiem and T. A. Costi, “Time Evolution of the Kondo Resonance in Response to a Quench,” *Phys. Rev. Lett.* **119**, 156601 (2017).
- [89] N. Roch, S. Florens, T. A. Costi, W. Wernsdorfer, and F. Balestro, “Observation of the Underscreened Kondo Effect in a Molecular Transistor,” *Phys. Rev. Lett.* **103**, 197202 (2009).
- [90] J. Parks et al., “Mechanical control of spin states in spin-1 molecules and the underscreened Kondo effect,” *Science* **328**, 1370 (2010).

Supplemental Material for

**Simulating Non-Markovian Open Quantum Dynamics with
Neural Quantum States**

Long Cao,^{1,*} Liwei Ge,^{1,*} Daochi Zhang,² Xiang Li,¹ Jialin Pan,¹
Yao Wang,¹ Rui-Xue Xu,^{1,3} YiJing Yan,¹ and Xiao Zheng^{2,3,†}

¹*Hefei National Research Center for Physical Sciences at the Microscale,
University of Science and Technology of China, Hefei, Anhui 230026, China*

²*Department of Chemistry, Fudan University, Shanghai 200438, China*

³*Hefei National Laboratory, Hefei, Anhui 230088, China*

(Dated: March 10, 2026)

CONTENTS

S1. Quantum dynamical equations for many-body open quantum systems	S2
S1.1. Open quantum system coupled to fermionic environment	S2
S1.2. Characterizing the non-Markovian memory of environment	S2
S1.3. Detailed forms of fermionic HEOM and DQME	S3
S2. Neural quantum state representation of RDT	S5
S3. Exploiting the sparsity of RDT	S6
S4. Temporal evolution of neural network parameters	S7
S5. Evaluation of physical quantities	S9
S6. Details of numerical calculations	S10
S6.1. Energetic parameters of OQSs and RBM hyperparameters	S10
S6.2. Monte Carlo sampling for the space of visible states	S11
S6.3. Numerical accuracy of the NQS-DQME results	S13
S6.4. Visualizing the evolution of RBM parameters	S15
S7. Comparing the performance of NQS-DQME to MPS-HEOM	S16
References	S17

* These authors contributed equally to this work.

† xzheng@fudan.edu.cn

S1. QUANTUM DYNAMICAL EQUATIONS FOR MANY-BODY OPEN QUANTUM SYSTEMS

S1.1. Open quantum system coupled to fermionic environment

We consider an open quantum system (OQS) in which the system is linearly coupled to the environment consisting of several noninteracting fermionic particle reservoirs. The Hamiltonian of the total system is described by (with $e = \hbar = 1$)

$$H_{\text{T}} = H_{\text{S}} + H_{\text{E}} + H_{\text{SE}}, \quad (\text{S1})$$

$$H_{\text{E}} = \sum_{\alpha} \sum_k \epsilon_{\alpha k} \hat{d}_{\alpha k}^{\dagger} \hat{d}_{\alpha k}, \quad (\text{S2})$$

$$H_{\text{SE}} = \sum_{\nu=1}^{N_{\text{S}}} \sum_{\alpha} \left(\hat{c}_{\nu}^{\dagger} \hat{F}_{\alpha\nu} + \hat{F}_{\alpha\nu}^{\dagger} \hat{c}_{\nu} \right), \quad (\text{S3})$$

where H_{S} represents the system of primary interest, H_{E} denotes the environment, and H_{SE} describes the system-environment coupling. In these terms, \hat{c}_{ν}^{\dagger} (\hat{c}_{ν}) denotes the creation (annihilation) operator for the ν -th single-particle state of the system, $\hat{d}_{\alpha k}^{\dagger}$ ($\hat{d}_{\alpha k}$) denotes the creation (annihilation) operator for the k -th single-particle state of the α -th reservoir, where the indices ν and k include the spin degree of freedom. $\hat{F}_{\alpha\nu} = \sum_k t_{\nu\alpha k} \hat{d}_{\alpha k}$, where $\hat{d}_{\alpha k}^{\dagger}$ ($\hat{d}_{\alpha k}$) represents the particle creation (annihilation) operator for the k -th single-particle state of α -reservoir, and $t_{\nu\alpha k}$ denotes the coupling strength between the system's ν -th state and the α -reservoir's k -th state.

S1.2. Characterizing the non-Markovian memory of environment

The hybridization spectral functions of the α -reservoir are defined as

$$J_{\alpha\nu}(\omega) \equiv \pi \sum_k |t_{\nu\alpha k}|^2 \delta(\omega - \epsilon_{\alpha k}). \quad (\text{S4})$$

In this work, we adopt a Lorentzian form for the hybridization spectral functions, i.e.,

$$J_{\alpha\nu}(\omega) = \frac{\Gamma_{\nu\alpha} W_{\alpha}^2}{(\omega - \Omega_{\alpha})^2 + W_{\alpha}^2}. \quad (\text{S5})$$

Here, $\Gamma_{\nu\alpha}$ is the hybridization strength between the system's ν -th state and the α -reservoir, $\Gamma_{\nu} = \sum_{\alpha} \Gamma_{\nu\alpha}$, and Ω_{α} and W_{α} are the band center and width of the α -reservoir, respectively. For simplicity, we take $\Omega_{\alpha} = \mu_{\alpha}$, where μ_{α} is the chemical potential of the α -reservoir. In particular, we set $\mu_{\alpha}^{\text{eq}} = 0$ in thermal equilibrium.

Since a reservoir of noninteracting fermionic particles linearly coupled to the system follows Gaussian statistics, its influence on the reduced system dynamics is entirely captured by the reservoir hybridization correlation functions, which are defined as

$$\begin{aligned} C_{\alpha\nu}^{+}(t - \tau) &\equiv \langle \hat{F}_{\alpha\nu}^{\dagger}(t) \hat{F}_{\alpha\nu}(\tau) \rangle_{\text{E}}, \\ C_{\alpha\nu}^{-}(t - \tau) &\equiv \langle \hat{F}_{\alpha\nu}(t) \hat{F}_{\alpha\nu}^{\dagger}(\tau) \rangle_{\text{E}}, \end{aligned} \quad (\text{S6})$$

where $\hat{F}_{\alpha\nu}(t) = e^{iH_E t} \hat{F}_{\alpha\nu} e^{-iH_E t}$, and $\langle \cdot \rangle_E = \text{tr}(\cdot \rho_E^{\text{eq}})$ with ρ_E^{eq} being the density matrix of the decoupled environment in thermal equilibrium. The reservoir correlation functions are related to the hybridization spectral functions through the fluctuation-dissipation theorem

$$C_{\alpha\nu}^{\sigma}(t) = \int_{-\infty}^{\infty} d\omega e^{\sigma i\omega t} f_{\alpha}^{\sigma}(\omega) J_{\alpha\nu}(\omega), \quad (\text{S7})$$

where $f_{\alpha}^{\sigma}(\omega) = 1/(1 + e^{\sigma\beta_{\alpha}(\omega - \mu_{\alpha})})$, and $\beta_{\alpha} = 1/(k_B T)$ is the inverse temperature of the α -reservoir. By employing a sum-over-poles expansion for $f_{\alpha}^{\sigma}(\omega)$ and $J_{\alpha\nu}(\omega)$, the reservoir correlation functions can be expressed as a linear combination of exponential functions

$$C_{\alpha\nu}^{\sigma}(t) = \sum_{p=1}^P \eta_{\alpha\nu p}^{\sigma} e^{-\gamma_{\alpha\nu p}^{\sigma} t}. \quad (\text{S8})$$

The j index used in the main text corresponds to the multi-index $\{\alpha\nu p\}$ here. For the benchmark tests presented in the main text, the Padé spectral decomposition scheme [1] is employed to carry out the exponential expansion in Eq. (S8).

When a time-dependent voltage is applied to the α -reservoir, the energy levels and chemical potential of the reservoir experiences a homogeneous shift $\Delta\mu_{\alpha}(t)$, which introduces a phase factor to the non-stationary reservoir correlation functions:

$$\tilde{C}_{\alpha\nu}^{\sigma}(t, \tau) = \exp\left[\sigma i \int_{\tau}^t dt' \Delta\mu_{\alpha}(t')\right] C_{\alpha\nu}^{\sigma}(t - \tau). \quad (\text{S9})$$

The two-time hybridization correlation functions $\tilde{C}_{\alpha\nu}^{\sigma}(t, \tau)$ serve as the memory kernel that explicitly express the non-Markovian memory content of the α -reservoir. Equations (S8) and (S9) provide the foundation for several numerically exact theories, such as the hierarchical equations of motion (HEOM) method and the dissipaton-embedded quantum master equation (DQME) in a second quantized form, for characterizing non-Markovian dissipative dynamics of many-body OQs.

S1.3. Detailed forms of fermionic HEOM and DQME

The basic variables of HEOM are the auxiliary density operators (ADOs) [2]. In the path-integral formulation, ADOs are defined by acting Grassmannian generating fields $\{\mathcal{B}_j^{\sigma}\}$ on the initial-time reduced density operator (RDO) ρ_0 , as follows [3]

$$\begin{aligned} \rho_{p_1 \dots p_I q_1 \dots q_J}^{(-\dots - + \dots +)} &\equiv (-1)^{(I+J)} \int_{t_0}^t \mathcal{D}\mathbf{x} \mathcal{D}\mathbf{x}' e^{iS_f[\mathbf{x}]} e^{-iS_b[\mathbf{x}']} \\ &\times e^{-\Phi[\mathbf{x}, \mathbf{x}']} \mathcal{B}_{p_1}^{-} \dots \mathcal{B}_{p_I}^{-} \mathcal{B}_{q_1}^{+} \dots \mathcal{B}_{q_J}^{+} \rho_0. \end{aligned} \quad (\text{S10})$$

Here, S_f and S_b denote forward and backward action functionals, respectively, Φ is the Feynman-Vernon influence functional, and \mathcal{B}_j^{-} (\mathcal{B}_j^{+}) represents the transfer of a fermionic particle from the system (environment) to the environment (system) via the j -th dissipation level, where j is an abbreviation for the multi-index $\{\alpha\nu p\}$. Because of the Grassmann

anti-symmetry inherent to fermions, interchanging any two \mathcal{B}_j^σ fields in Eq. (S10) yields a minus sign.

With the exponential decomposition of reservoir memory in Eq. (S8), the HEOM are expressed as

$$\begin{aligned} \dot{\rho}_{p_1 \dots p_I q_1 \dots q_J}^{(-\dots - + \dots +)} &= \left[-i\mathcal{L}_s + \sum_j \gamma_j \right] \rho_{p_1 \dots p_I q_1 \dots q_J}^{(-\dots - + \dots +)} \\ &+ \sum_{r=1}^I \mathcal{C}_{p_r}^- \rho_{p_1 \dots p_{r-1} p_{r+1} \dots q_J}^{(-\dots - - \dots +)} + \sum_{r=1}^J \mathcal{C}_{q_r}^+ \rho_{p_1 \dots q_{r-1} q_{r+1} \dots q_J}^{(-\dots + + \dots +)} \\ &+ \sum_j \mathcal{A}_j^- \rho_{p_1 \dots p_I j q_1 \dots q_J}^{(-\dots - - + \dots +)} + \sum_j \mathcal{A}_j^+ \rho_{p_1 \dots p_I j q_1 \dots q_J}^{(-\dots - + + \dots +)}. \end{aligned} \quad (\text{S11})$$

Here, $\mathcal{L}_s = [H_s, \cdot]$ denotes the system Liouvillian, and \mathcal{A}_j^σ and \mathcal{C}_p^σ are tier-up and tier-down superoperators acting on the ADOs, respectively.

The DQME theory provides a fresh viewpoint on the ADOs. The entire set of ADOs is mapped onto the reduced density tensor (RDT) of the dissipaton-embedded system, denoted as ρ . Specifically, the mapping from an ADO to an element of the RDT is given by

$$\rho_{p_1 \dots p_I q_1 \dots q_J}^{(-\dots - + \dots +)} \mapsto \rho(\vec{n}, \vec{n}'; \vec{m}^-, \vec{m}^+), \quad (\text{S12})$$

where each of the vectors \vec{n} and \vec{n}' corresponds to a fermionic particle configuration for the system, while \vec{m}^σ represents a dissipaton configuration.

The formal equivalence between the HEOM and DQME is established by writing the equation of motion for each element of the RDT, as follows,

$$\begin{aligned} \dot{\rho}(\vec{n}, \vec{n}'; \vec{m}^-, \vec{m}^+) &= -i \sum_{\vec{k}} \left[H_s(\vec{n}, \vec{k}) \rho(\vec{k}, \vec{n}', \vec{m}^-, \vec{m}^+) - \rho(\vec{n}, \vec{k}, \vec{m}^-, \vec{m}^+) H_s(\vec{k}, \vec{n}') \right] \\ &+ \sum_j (\gamma_j^- m_j^- + \gamma_j^+ m_j^+) \rho(\vec{n}, \vec{n}'; \vec{m}^-, \vec{m}^+) \\ &- i \sum_j (-1)^{\sum_{k>j} m_k^-} \sum_{\vec{k}} \left[c_\nu^*(\vec{k}, \vec{n}) \rho(\vec{k}, \vec{n}', \vec{m}_{j+}^-, \vec{m}^+) - (-1)^{M^- + M^+} \rho(\vec{n}, \vec{k}, \vec{m}_{j+}^-, \vec{m}^+) c_\nu^*(\vec{n}', \vec{k}) \right] \\ &- i \sum_j (-1)^{\sum_{k<j} m_k^+} \sum_{\vec{k}} \left[(-1)^{M^- + M^+} c_\nu(\vec{n}, \vec{k}) \rho(\vec{k}, \vec{n}', \vec{m}^-, \vec{m}_{j+}^+) - \rho(\vec{n}, \vec{k}, \vec{m}^-, \vec{m}_{j+}^+) c_\nu(\vec{k}, \vec{n}') \right] \\ &- i \sum_j (-1)^{\sum_{k<j} m_k^-} \sum_{\vec{k}} \left[(-1)^{M^- - 1} \eta_j^{(-)} c_\nu(\vec{n}, \vec{k}) \rho(\vec{k}, \vec{n}', \vec{m}_{j-}^-, \vec{m}^+) \right. \\ &\quad \left. - (-1)^{M^+} [\eta_j^{(+)}]^* \rho(\vec{n}, \vec{k}, \vec{m}_{j-}^-, \vec{m}^+) c_\nu(\vec{k}, \vec{n}') \right] \\ &- i \sum_j (-1)^{\sum_{k>j} m_k^+} \sum_{\vec{k}} \left[(-1)^{M^-} \eta_j^{(+)} c_\nu^*(\vec{k}, \vec{n}) \rho(\vec{k}, \vec{n}', \vec{m}^-, \vec{m}_{j-}^+) \right. \\ &\quad \left. - (-1)^{M^+ - 1} [\eta_j^{(-)}]^* \rho(\vec{n}, \vec{k}, \vec{m}^-, \vec{m}_{j-}^+) c_\nu^*(\vec{n}', \vec{k}) \right] \end{aligned} \quad (\text{S13})$$

where $M^\sigma = \sum_k m_k^\sigma$, $c_\nu(\vec{n}, \vec{n}')$ denotes the matrix representation of the annihilation operator \hat{c}_ν , with ν belonging to the multi-index $j = \{\alpha\nu p\}$, and $\vec{m}_{j+(-)}^\sigma$ indicates that adding (subtracting) a dissipaton to (from) the j -th level in the dissipaton configuration \vec{m}^σ .

S2. NEURAL QUANTUM STATE REPRESENTATION OF RDT

In the restricted Boltzmann machine (RBM) presentation, the auxiliary wavefunctions are expressed as

$$\begin{aligned}
\psi(\vec{n}; \vec{m}; \vec{a}) &= \sum_{\{\vec{h}\}} \exp\left(\mathbf{a}^T \mathbf{b} + \mathbf{h}^T \mathbf{g} + \mathbf{n}^T \mathbf{c} + \mathbf{m}^T \mathbf{d} \right. \\
&\quad \left. + \mathbf{n}^T \mathbf{X} \mathbf{h} + \mathbf{n}^T \mathbf{X}' \mathbf{a} + \mathbf{m}^T \mathbf{Y} \mathbf{h} + \mathbf{m}^T \mathbf{K} \mathbf{a} + \mathbf{n}^T \mathbf{D} \mathbf{m}\right) \\
&= \exp\left(\mathbf{a}^T \mathbf{b} + \mathbf{n}^T \mathbf{c} + \mathbf{m}^T \mathbf{d} + \mathbf{n}^T \mathbf{X}' \mathbf{a} \mathbf{m}^T \mathbf{K} \mathbf{a} + \mathbf{n}^T \mathbf{D} \mathbf{m}\right) \\
&\quad \times \prod_j \left[1 + \exp\left(g_j + \sum_i n_i X_{ij} + \sum_i m_i Y_{ij}\right) \right], \tag{S14}
\end{aligned}$$

$$\begin{aligned}
\varphi(\vec{n}'; \vec{m}; \vec{a}) &= \sum_{\{\vec{h}\}} \exp\left(\mathbf{a}^T \mathbf{b} + \mathbf{h}^T \mathbf{g} + \mathbf{n}'^T \mathbf{c} + \mathbf{m}^T \mathbf{d} \right. \\
&\quad \left. + \mathbf{n}'^T \mathbf{X} \mathbf{h} + \mathbf{n}'^T \mathbf{X}' \mathbf{a} + \mathbf{m}^T \mathbf{Y}' \mathbf{h} + \mathbf{m}^T \mathbf{K} \mathbf{a} + \mathbf{n}'^T \mathbf{D} \mathbf{m}\right) \\
&= \exp\left(\mathbf{a}^T \mathbf{b} + \mathbf{n}'^T \mathbf{c} + \mathbf{m}^T \mathbf{d} + \mathbf{n}'^T \mathbf{X}' \mathbf{a} + \mathbf{m}^T \mathbf{K} \mathbf{a} + \mathbf{n}'^T \mathbf{D} \mathbf{m}\right) \\
&\quad \times \prod_j \left[1 + \exp\left(g_j + \sum_i n'_i X_{ij} + \sum_i m_i Y'_{ij}\right) \right]. \tag{S15}
\end{aligned}$$

Here, each of the vectors \vec{n} and \vec{n}' corresponds to fermionic particle configuration of the system, while \vec{m} represents a dissipaton configuration; \vec{a} and \vec{h} denote a set of auxiliary nodes and hidden nodes, respectively; $(\mathbf{b}, \mathbf{c}, \mathbf{d}, \mathbf{g})$ and $(\mathbf{D}, \mathbf{K}, \mathbf{X}, \mathbf{X}', \mathbf{Y}, \mathbf{Y}')$ represent the bias vectors and weight matrices of RBMs, respectively. Then, the neural quantum state (NQS) representation for the RDT of the DQME theory is established as

$$\begin{aligned}
\rho_{\text{pre}}(\vec{n}, \vec{n}'; \vec{m}) &= \sum_{\{\vec{a}\}} \psi(\vec{n}; \vec{m}; \vec{a}) \varphi^*(\vec{n}'; \vec{m}; \vec{a}) \\
&= \exp\left[\sum_i (d_i + d_i^*) m_i + \sum_i (c_i n_i + c_i^* n'_i) + \mathbf{n}^T \mathbf{D} \mathbf{m} + \mathbf{n}'^T \mathbf{D}'^* \mathbf{m}\right] \\
&\quad \times \prod_j \left[1 + \exp\left(b_j + b_j^* + \sum_i n_i X'_{ij} + \sum_i n'_i X'^*_{ij} + \sum_i m_i (K_{ij} + K^*_{ij})\right) \right] \\
&\quad \times \prod_j \left[1 + \exp\left(g_j + \sum_i n_i X_{ij} + \sum_i m_i Y_{ij}\right) \right] \\
&\quad \times \prod_j \left[1 + \exp\left(g_j^* + \sum_i n'_i X^*_{ij} + \sum_i m_i Y'^*_{ij}\right) \right]. \tag{S16}
\end{aligned}$$

In Eqs. (S14)-(S16), ψ and φ share the same weights associated with the visible nodes representing the system particle configurations (the \vec{n} nodes). This preserves the Hermiticity and positivity of the RDO.

The RDT is subject to the following symmetry constraint:

$$\rho(\vec{s}) = (-1)^{[M^-/2] + [M^+/2]} \rho^*(\vec{s}^T), \tag{S17}$$

where $\lfloor \cdot \rfloor$ denotes the floor function, $M^\sigma = \sum_j m_j^\sigma$, and m_j^σ is the j -th element of \vec{m}^σ . Here, $\vec{s} \equiv (\vec{n}, \vec{n}'; \vec{m}^-, \vec{m}^+)$ represents a visible state, while $\vec{s}^T \equiv (\vec{n}', \vec{n}; \vec{m}^+, \vec{m}^-)$ is its block-swapped counterpart. We enforce the symmetry constraint by constructing

$$\rho_{\text{sym}}(\vec{s}) = \rho_{\text{pre}}(\vec{s}) + (-1)^{\lfloor M^-/2 \rfloor + \lfloor M^+/2 \rfloor} \rho_{\text{pre}}^*(\vec{s}^T). \quad (\text{S18})$$

The number of real-valued parameters in the RBM is

$$N_{\text{para}} = 2N_{\text{h}} + N_{\text{a}} + 2(1 + N_{\text{h}} + N_{\text{a}})N_{\text{s}} + (1 + 4N_{\text{h}} + N_{\text{a}})N_{\text{e}} + 4N_{\text{e}}N_{\text{s}}. \quad (\text{S19})$$

S3. EXPLOITING THE SPARSITY OF RDT

Harnessing the sparsity of the RDT significantly enhances the numerical efficiency of the NQS-DQME approach. This is because a substantial portion of the RDT elements, represented by the visible states \vec{s} of the RBM, are inherently zero. Identifying and excluding these zero-valued elements during sum-over-states operations substantially reduces the computational cost of NQS-DQME.

The sparsity pattern of the RDT is determined by the forms of H_{s} and H_{SE} . To establish this pattern, we categorize all visible states \vec{s} based on the characteristic vector $\mathbf{u}(\vec{s})$, defined as $u_\nu = (M_\nu^+ - M_\nu^-) + (n_\nu - n'_\nu)$, where $\nu = 1, \dots, N_{\text{s}}$, and $M_\nu^\sigma = \sum_{\alpha p} m_{\alpha\nu p}^\sigma$. Visible states associated with the same \mathbf{u} -vector belong to the same category. In cases where a category includes an RDO element (i.e., $\rho(\vec{n}, \vec{n}'; \vec{m} = \vec{0})$), then $\rho(\vec{s}) = 0$ for all \vec{s} in that category, provided the matrix element $\langle \vec{n}' | \exp(-H_{\text{s}}) | \vec{n} \rangle = 0$. Conversely, if a category contains no RDO element, then $\rho(\vec{s}) = 0$ for all \vec{s} in that category.

The establishment of the sparsity pattern enables the implementation of an efficient filter, denoted as $f_{\text{spa}}(\vec{s})$, which allows for rapid screening of visible states before processing in the NQS-DQME solver. This filter promptly returns a value of 0 if $\rho(\vec{s})$ is determined to be zero-valued based on the aforementioned rules.

The efficiency of the sparsity filter is demonstrated in Table S1. The filter reduces the number of non-zero elements in the RDT by approximately an order of magnitude across a range of temperatures, leading to a significant reduction in computational cost.

TABLE S1. Reduction of dynamical variables via the sparsity filter for the single-impurity system (Case 1). The number of non-zero RDT elements, N_{RDT} , is shown with and without the application of the sparsity filter for different temperatures.

$k_{\text{B}}T/\Gamma$	3.0	2.0	1.0	0.6	0.3
N_{RDT} (full)	52880	99536	167760	261648	385296
N_{RDT} (filtered)	6724	12884	21988	34612	51332
Reduction Factor	7.9	7.7	7.6	7.6	7.5

S4. TEMPORAL EVOLUTION OF NEURAL NETWORK PARAMETERS

The DQME can be formally recast into a compact form of

$$\dot{\boldsymbol{\rho}} = \mathcal{L}\boldsymbol{\rho}, \quad (\text{S20})$$

where \mathcal{L} represents a generalized Liouvillian of the dissipaton-embedded system. In the NQS representation, the temporal evolution of $\boldsymbol{\rho}$ is transformed into the evolution of the time-dependent parameters of the neural network $\{\boldsymbol{\alpha}(t)\}$, i.e.,

$$\dot{\boldsymbol{\rho}} \simeq \sum_k \dot{\alpha}_k \frac{\partial \boldsymbol{\rho}}{\partial \alpha_k}. \quad (\text{S21})$$

Here, $\frac{\partial \boldsymbol{\rho}}{\partial \alpha_k}$ are obtained through analytic differentiation, and the values of $\dot{\alpha}_k$ are determined by applying the time-dependent variational principle (TDVP) [4], which minimizes the 2-norm loss function:

$$\Delta s^2 = \left\| \sum_k \dot{\alpha}_k \hat{O}^k \boldsymbol{\rho} - \mathcal{L}\boldsymbol{\rho} \right\|_2^2, \quad (\text{S22})$$

where $\hat{O}^k \equiv \frac{\partial}{\partial \alpha_k}$. Minimizing Δs^2 involves solving the linear equation

$$\sum_k \mathcal{S}_{l,k} \dot{\alpha}_k = \mathcal{F}_l, \quad (\text{S23})$$

where

$$\mathcal{S}_{l,k} = \overline{O_l^* O_k} + \overline{O_k^* O_l} = 2 \operatorname{Re} (\overline{O_l^* O_k}), \quad (\text{S24})$$

$$\mathcal{F}_l = \overline{O_l^* \mathcal{L}_{\text{loc}}} + \overline{\mathcal{L}_{\text{loc}}^* O_l} = 2 \operatorname{Re} (\overline{O_l^* \mathcal{L}_{\text{loc}}}), \quad (\text{S25})$$

with the definitions:

$$\overline{AB} \equiv \sum_{\{\vec{s}\}} A(\vec{s}) B(\vec{s}), \quad (\text{S26})$$

$$O_k(\vec{s}) \equiv \frac{\partial \rho(\vec{s})}{\partial \alpha_k}, \quad (\text{S27})$$

$$\mathcal{L}_{\text{loc}}(\vec{s}) \equiv \langle \vec{s} | \mathcal{L} | \boldsymbol{\rho} \rangle. \quad (\text{S28})$$

At each time step, Eq. (S23) is solved either directly by regularizing the matrix \mathcal{S} (adding a small positive constant $\delta \sim 10^{-12} - 10^{-8}$ to its diagonal elements to eliminate its singularity), or iteratively using the minimum residual quadratic linear problem (MINRES-QLP) algorithm [5]. The resulting time derivatives $\{\dot{\alpha}_k\}$ are then used to update $\{\alpha_k\}$ via the fourth-order Runge-Kutta (RK4) algorithm. However, solving Eq. (S23) with high accuracy at each time step is computationally demanding for complex systems, representing a major bottleneck in the current NQS-DQME implementation.

The implementation of TDVP typically requires a Markov chain Monte Carlo (MCMC) sampling algorithm [6] to perform the sum-over-states operations. In this work, inspired by the dissipaton occupation number truncation in the fermionic DQME method, we limit the

sampling to a truncated visible-state space with a maximum allowed occupancy of dissipatons set to M_{\max} . Consequently, any RDT elements $\rho(\vec{s})$ with $M(\vec{s}) = \sum_{\sigma_j} m_j^\sigma > M_{\max}$ are enforced to be zero and automatically excluded from the MCMC sampling. Additionally, the sparsity filter $f_{\text{spa}}(\vec{s})$ introduced in Section S3 further accelerates the sampling procedure.

Based on extensive applications of the HEOM method, it has been found that ADOs at lower tiers hold relatively greater significance and less amount compared to those at higher tiers. In the context of DQME, this suggests that the sampling procedure should prioritize the RDT elements associated with lower dissipaton occupancy. Based on this notion, we design a MCMC sampling protocol that is compatible with the NQS-DQME framework, which proceeds as follows.

The set of accessible states $Q = \{\vec{s} \mid M(\vec{s}) \leq M_{\max}\}$ partitions into two subsets, the traversed states Q_1 and the sampling subset Q_2 , where $Q_1 = \{\vec{s} \mid M(\vec{s}) \leq L\}$ with $L < M_{\max}$ and $Q_2 = Q \setminus Q_1$. The sum-over-states operation is then carried out as

$$\sum_{\{\vec{s}\}} A(\vec{s}) \simeq \sum_{\vec{s} \in Q} A(\vec{s}) = \sum_{\vec{s} \in Q_1} A(\vec{s}) + \sum_{\vec{s} \in Q_2} A(\vec{s}). \quad (\text{S29})$$

Here, summing over the Q_1 subset is straightforward and does not require any sampling due to its small size. For the sum over the Q_2 subset, the following equation is used:

$$\sum_{\vec{s} \in Q_2} A(\vec{s}) = \sum_{\vec{s} \in Q_2} \tilde{p}(\vec{s}) \frac{A(\vec{s})}{\tilde{p}(\vec{s})} = Z_p \left\langle \frac{A(\vec{s})}{\tilde{p}(\vec{s})} \right\rangle_{Q_2}. \quad (\text{S30})$$

Unlike conventional quantum Monte Carlo methods, where the distribution function $\tilde{p}(\vec{s})$ is typically determined by the normalized wavefunction or density matrix, here the unnormalized RDT employs $\tilde{p}(\vec{s}) = e^{-\lambda M(\vec{s})}$ for sampling in the Q_2 space, with the empirical parameter $\lambda = 3$. The average of $X(\vec{s})$ over the Q_2 subset is computed as $\langle X(\vec{s}) \rangle_{Q_2} = \sum_{\vec{s} \in Q_2} X(\vec{s}) p(\vec{s})$, where $p(\vec{s}) = \tilde{p}(\vec{s})/Z_p$, with $Z_p = \sum_{\vec{s} \in Q_2} \tilde{p}(\vec{s})$ being the partition function. To navigate through the Q_2 space efficiently, the MCMC walker proposes a new state \vec{s}' from the current state \vec{s} by flipping a pair of elements (0 to 1 or 1 to 0 interchangeably) using one of two randomly chosen rules: (i) simultaneously flip both m_j^+ and m_j^- for a given j , or (ii) simultaneously flip m_j^+ (or m_j^-) and its corresponding n_ν (or n'_ν), where ν belongs to the multi-index j .

The Metropolis-Hastings criterion [7] is then applied to accept or reject the proposed move, ensuring convergence to the target distribution.

To illustrate the source of the high efficiency of this sampling method, we compute the variance of the sampled quantity $\sum_{\vec{s} \in Q} A(\vec{s})$. First, we define the random variables $A_{2,i}$ and A_2 :

$$P \left(A_{2,i} = \frac{A(\vec{s})}{\tilde{p}(\vec{s})} \right) = p(\vec{s}), \quad (\text{S31})$$

$$A_2 = \frac{1}{N_{\text{MC}}} \sum_{i=1}^{N_{\text{MC}}} A_{2,i}. \quad (\text{S32})$$

Here, $A_{2,i}$ denotes the N_{MC} independent identically distributed random variables obtained from MC sampling. The value we compute via MC sampling is actually the random variable A :

$$A = A_1 + Z_p * A_2, \quad (\text{S33})$$

where $A_1 = \sum_{\vec{s} \in Q_1} A(\vec{s})$. It is easy to see that:

$$\sum_{\vec{s} \in Q} A(\vec{s}) = E[A], \quad (\text{S34})$$

where $E[A]$ denotes the expectation value of A . The efficiency of this sampling can be characterized by the variance of the random variable A :

$$\text{Var}(A) = Z_p^2 * \frac{\text{Var}(A_{2,i})}{N_{\text{MC}}}. \quad (\text{S35})$$

It can be seen that as the sampling truncation L for Q_2 increases, Z_p decreases; moreover, since the value of $A(\vec{s})$ often significantly decreases with increasing occupation number of dissipatons, $\text{Var}(A_{2,i})$ also decreases as L increases. In contrast, conventional full-space MC sampling corresponds to a truncation $L = -1$. Therefore, for the same number of samples, the variance of this sampling method is smaller than that of conventional full-space MC sampling, indicating that it has higher sampling efficiency. The Table S2 shows the variance of the sampled quantity $\|\mathcal{L}\rho\|_2^2$ at the beginning of the temporal evolution against the sampling truncation L in the Case 1 at the $k_{\text{B}}T = 0.3\Gamma$, where $A(\vec{s}) = |(\mathcal{L}\rho)(\vec{s})|^2$. This table demonstrates that the our sampling strategy with the sampling truncation $L = 2$ can achieve the same variance as the full space MC sampling with a sampling number four orders of magnitude smaller, rendering the remarkable smooth evolution curve in Fig. 3(b). This strategy can be extended to spin-lattice systems and quantum chemistry by combining a direct summation of the mean-field results and low-excitation configurations with Monte Carlo sampling of the high-excitation configurations.

TABLE S2. The variance of the sampled $\|\mathcal{L}\rho\|_2^2$ at $t = 0./\Gamma$ in Case 1 at the $k_{\text{B}}T = 0.3$.

L	-1	0	1	2
Z_p	23.93	19.93	13.55	5.94
$\text{Var}(A_{2,i})$	$3.09 * 10^{-3}$	$3.68 * 10^{-3}$	$1.9313 * 10^{-4}$	$8.98 * 10^{-6}$
$Z_p^2 \text{Var}(A_{2,i})$	1.76	1.46	$3.55 * 10^{-2}$	$3.17 * 10^{-4}$

When the open quantum dynamics begins from an equilibrium state of the full system, the initial parameters $\alpha(t_0)$ are determined by minimizing the $\|\mathcal{L}\rho_\alpha\|_2^2$ or by evolving a random initial state to the long-time limit.

S5. EVALUATION OF PHYSICAL QUANTITIES

With the RDT obtained using the NQS-DQME solver, a wide range of physical observables of experimental relevance can be evaluated. In the following, we explicitly include

the spin index s . Thus, the index ν used in the preceding sections and from the main text now extends to νs , and the multi-index becomes $j = \{\alpha\nu sp\}$. For instance, the occupation number of spin- s electrons on the ν -th impurity ($n_{\nu s}$), the inter-impurity spin correlation (S_{12}), and the von Neumann entropy (S_{vN}) are calculated based on the RDO, $\rho_0(\vec{n}, \vec{n}') = \rho(\vec{n}, \vec{n}'; \vec{m} = \vec{0})$, as follows:

$$\begin{aligned} n_{\nu s} &= \text{tr}_s(\hat{n}_{\nu s}\rho_0), \\ S_{12} &= \text{tr}_s(\hat{\mathbf{S}}_1 \cdot \hat{\mathbf{S}}_2\rho_0), \\ S_{\text{vN}} &= -\text{tr}_s(\rho_0 \log \rho_0), \end{aligned} \quad (\text{S36})$$

where $\hat{n}_{\nu s} = \hat{c}_{\nu s}^\dagger \hat{c}_{\nu s}$, and $\hat{\mathbf{S}}_\nu = \frac{1}{2} \sum_{ss'} \hat{c}_{\nu s}^\dagger \boldsymbol{\sigma}_{ss'} \hat{c}_{\nu s'}$ with $\boldsymbol{\sigma} = (\sigma_x, \sigma_y, \sigma_z)$ the Pauli matrices.

The electric current flowing into α -reservoir (I_α) and impurity-reservoir hybridization energy (E_{hyb}) are calculated using the RDT elements with $M(\vec{s}) = 1$ as follows:

$$I_\alpha = -2 \text{Im} \left\{ \sum_{\nu sp} \sum_{\vec{n}, \vec{n}'} \langle \vec{n}' | \hat{c}_{\nu s} | \vec{n} \rangle \rho(\vec{n}, \vec{n}'; \vec{m}_{\alpha\nu sp}^+, \vec{0}) \right\}, \quad (\text{S37})$$

$$E_{\text{hyb}} = 2 \text{Re} \left\{ \sum_{\alpha\nu sp} \sum_{\vec{n}, \vec{n}'} \langle \vec{n}' | \hat{c}_{\nu s} | \vec{n} \rangle \rho(\vec{n}, \vec{n}'; \vec{m}_{\alpha\nu sp}^+, \vec{0}) \right\}, \quad (\text{S38})$$

where $\vec{m}_{\alpha\nu sp}^+$ denotes the vector \vec{m}^+ with only one nonzero element, i.e., $m_{\alpha\nu sp}^+ = 1$.

S6. DETAILS OF NUMERICAL CALCULATIONS

S6.1. Energetic parameters of QoSs and RBM hyperparameters

In Case 1, the values of energetic parameters adopted are (in units of $\Gamma = (\Gamma_L + \Gamma_R)/2$): $\Gamma_L = \Gamma_R = 1$, $\epsilon_0 = U_0/2 = 2$, $\Delta\epsilon = -7$, $\Delta U = 6$, $W_L = W_R = 50$, $\Delta\mu_L = 0$, and $\Delta\mu_R = 0.5$.

In Case 2, the values of energetic parameters adopted are (in units of $\Gamma = \Gamma_1/2$): $\Gamma_1 = \Gamma_2 = 2$, $\epsilon_0 = -U_0/2 = -6$, $J = 8$, and $W = 20$.

The number of Padé poles employed to decompose the hybridization correlation functions, as well as the setting of RBM hyperparameters, for different temperatures in Cases 1 and 2 are given in Table S3 and Table S4, respectively.

TABLE S3. Number of Padé poles and RBM hyperparameters employed in Case 1.

$k_B T/\Gamma$	3.0	2.0	1.0	0.6	0.3
$P_{\text{Padé}}$	3	4	5	6	7
N_{h}	20	20	20	20	30
N_{a}	20	20	20	20	30
N_{para}	3712	4584	5456	7783	10510

The dimensions of the dissipaton-embedded system (number of system and dissipaton levels) in Cases 1 and 2 are shown in Tables S5 and S6, respectively. The number of dissipaton levels N_{E} increases as the temperature decreases, which is necessary to accurately capture the non-Markovian memory effects at lower temperatures.

TABLE S4. Number of Padé poles and RBM hyperparameters employed in Case 2.

$k_B T/\Gamma$	2.40	0.48	0.40	0.32	0.24
$P_{\text{Padé}}$	3	4	4	5	5
N_h	60	60	60	70	70
N_a	20	20	20	30	30
N_{para}	9652	11868	11868	16674	16674

TABLE S5. Dimensions of the dissipaton-embedded system for Case 1.

$k_B T/\Gamma$	3.0	2.0	1.0	0.6	0.3
N_s	2	2	2	2	2
N_E	32	40	48	56	64

S6.2. Monte Carlo sampling for the space of visible states

In our practical implementation, we employ a hybrid sampling strategy. The subspace of visible states $\{\vec{s}\}$ with $M(\vec{s}) \leq L$ (subspace Q_1) is fully enumerated, while the subspace with $L < M(\vec{s}) \leq M_{\text{max}}$ (subspace Q_2) is sampled using the MCMC algorithm. For both Case 1 and Case 2, we set $M_{\text{max}} = 3$ and $L = 2$, which ensures sufficient accuracy for the DQME calculations presented in this work. The sizes of the traversed space N_{Q_1} and the sampling space N_{Q_2} for all temperatures studied are provided in Table S7 and Table S8.

As shown in Fig. 3(d) of the main text, MCMC sampling with $N_{\text{MC}} = 4096$ states achieves high accuracy ($\mathcal{E}_{I_R} < 1\%$) even at the lowest temperature studied. This sampling size constitutes only a small fraction of the Q_2 subspace dimension ($N_{Q_2} = 48128$), demonstrating the high efficiency of our customized MCMC algorithm.

Figure S1 presents a comparison between the results obtained via MCMC sampling and the reference values from the HEOM method. Despite minor sampling errors, the MCMC approach maintains small relative errors: $\mathcal{E}_{S_{12}} \approx 0.7\%$ at $k_B T = 2.4\Gamma$ and $\mathcal{E}_{S_{12}} \approx 1.5\%$ at $k_B T = 0.24\Gamma$. The inset shows that the relative error decreases rapidly with increasing sample size N_{MC} , achieving a relatively low error $\mathcal{E}_{S_{12}} \approx 1.7\%$ with a small sampling number $N_{\text{MC}} = 12288$ compared to the full Q_2 space size $N_{Q_2} = 91008$.

TABLE S6. Dimensions of the dissipaton-embedded system for Case 2.

$k_B T/\Gamma$	2.40	0.48	0.40	0.32	0.24
N_S	4	4	4	4	4
N_E	32	40	40	48	48

TABLE S7. Size of the traversed space and the sampling space in Case 1.

$k_B T/\Gamma$	3.0	2.0	1.0	0.6	0.3
N_{Q_1}	836	1284	1828	2468	3204
N_{Q_2}	5888	11600	20160	32144	48128

TABLE S8. Size of the traversed space and the sampling space in Case 2.

$k_B T/\Gamma$	2.40	0.48	0.40	0.32	0.24
N_{Q_1}	3842	5898	5898	8394	8394
N_{Q_2}	26624	52400	52400	91008	91008

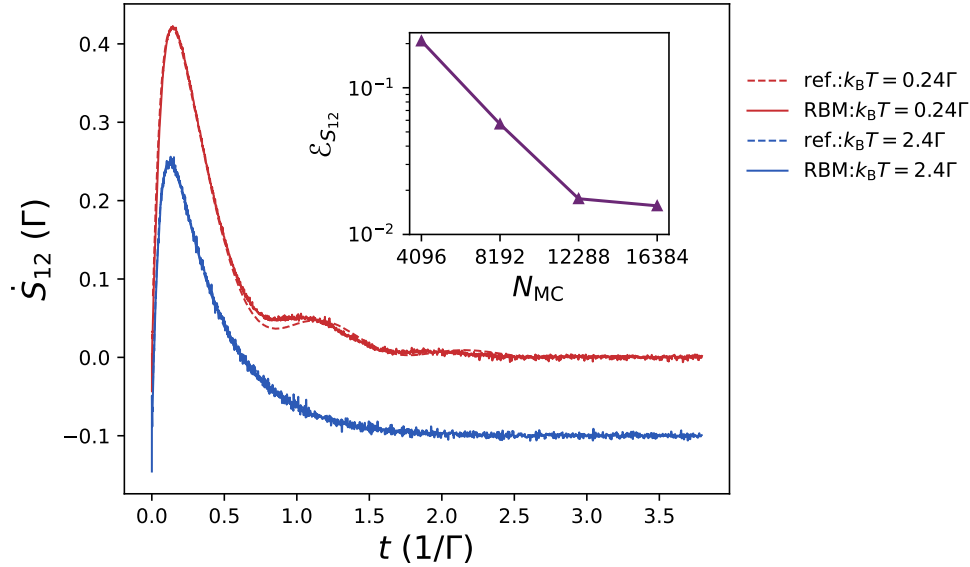


FIG. S1. Temporal evolution of $\dot{S}_{12}(t)$ at $k_B T = 2.4\Gamma$ and 0.24Γ in Case 2. The lines are vertically offset for clarity. Inset: variation of $\mathcal{E}_{S_{12}}$ with the sampling number N_{MC} at $k_B T = 0.24\Gamma$. RBM hyperparameters: $N_h = 70$ and $N_a = 30$.

S6.3. Numerical accuracy of the NQS-DQME results

Table S9 and Table S10 present the relative errors of key quantities for Cases 1 and 2, respectively, benchmarking the NQS-DQME results against reference HEOM data. A clear trend is observed: the relative errors generally increase as the temperature decreases, where non-Markovian effects become more pronounced. This trend underscores the growing challenge of accurately capturing quantum correlations in many-body OQSs as the environment's memory content increases.

Particularly, in Case 1 at the lowest temperature ($k_B T = 0.3\Gamma$), the relative error for $I_R(t)$ obtained via MCMC sampling (0.965%) is slightly lower than that from full sampling (0.998%). This minor discrepancy may be attributed to a partial cancellation between the errors introduced by the stochastic MCMC sampling and those inherent to the RBM representation itself.

TABLE S9. Relative errors of the NQS-DQME results for $I_R(t)$ and $n_\uparrow(t)$ in Case 1 with $t_{\text{lo}} = 3.8/\Gamma$.

Error	sampling	$k_B T/\Gamma$				
		3.0	2.0	1.0	0.6	0.3
\mathcal{E}_{I_R} (%)	full	0.020	0.047	0.108	0.400	0.998
\mathcal{E}_{n_\uparrow} (%)	full	0.000	0.001	0.016	0.032	0.027
\mathcal{E}_{I_R} (%)	MCMC	0.070	-	-	-	0.965
\mathcal{E}_{n_\uparrow} (%)	MCMC	0.001	-	-	-	0.047

TABLE S10. Relative errors of the NQS-DQME results for $S_{12}(t)$, $S_{vN}(t)$ and $E_{\text{hyb}}(t)$ in Case 2 with $t_{\text{lo}} = 3/\Gamma$.

Error	sampling	$k_B T/\Gamma$				
		2.40	0.48	0.40	0.32	0.24
$\mathcal{E}_{S_{12}}$ (%)	full	0.305	0.631	0.770	0.902	0.828
$\mathcal{E}_{S_{vN}}$ (%)	full	0.125	0.262	0.202	0.311	0.267
$\mathcal{E}_{E_{\text{hyb}}}$ (%)	full	0.049	0.212	0.123	0.156	0.286
$\mathcal{E}_{S_{12}}$ (%)	MCMC	0.746	-	-	-	1.567
$\mathcal{E}_{S_{vN}}$ (%)	MCMC	0.328	-	-	-	0.612
$\mathcal{E}_{E_{\text{hyb}}}$ (%)	MCMC	0.088	-	-	-	0.316

Figure S2 shows the spectral function $A(\omega) = A_{\nu s}(\omega) = \frac{1}{2\pi} \int dt e^{i\omega t} \langle \{\hat{c}_{\nu s}(t), \hat{c}_{\nu s}^\dagger\} \rangle$ for a localized impurity in Case 2. Comparing initial ($t = t_0$) and final ($t = t_{\text{lo}}$) states at temperatures $k_B T = 2.4\Gamma$ and 0.24Γ , we observe: (i) At low temperature ($k_B T = 0.24\Gamma$), the final state exhibits significant reduction of the Kondo peak height at $\omega = 0$. (ii) This reduction indicates that high-spin state formation in the two-impurity composite creates underscreened Kondo states with weakened impurity-reservoir correlations [8–10]. (iii) At high temperature ($k_B T = 2.4\Gamma$), thermal fluctuations completely suppress Kondo correlations.

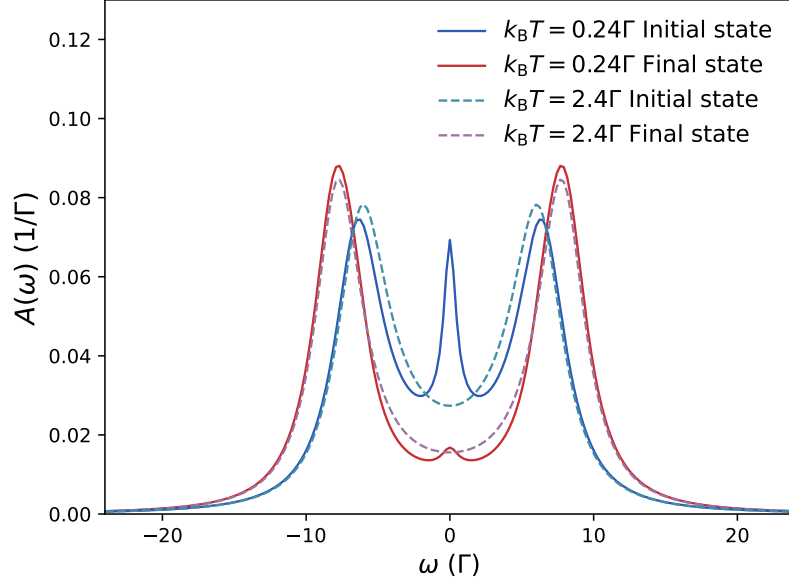


FIG. S2. Impurity spectral function in the initial and final states in Case 2.

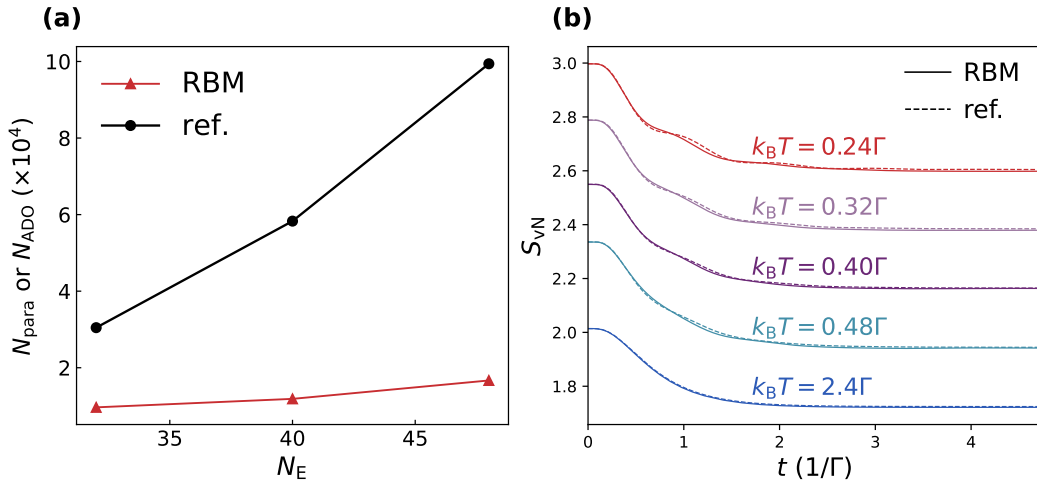


FIG. S3. (a) Number of explicitly accessed dynamical variables by the NQS-DQME and HEOM methods at various temperatures in Case 2, where the values of N_E correspond to the different temperatures; see Table S4 for details. (b) Temporal evolution of the von Neumann entropy S_{vN} at various temperatures in Case 2. The results obtained by the NQS-DQME are compared to the reference values from the HEOM method. The lines are vertically offset for clarity.

Figure S3(a) demonstrates that, similar to the trend shown in Fig. 3(e) of the main text, the NQS-DQME approach substantially reduces the number of dynamical variables required to describe non-Markovian dynamics compared to the HEOM method. Figure S3(b) depicts the temporal evolution of the von Neumann entropy $S_{\text{vN}}(t)$ at various temperatures in Case 2. It is evident that, regardless of the temperature, the final equilibrium state exhibits lower von Neumann entropy compared to the initial state, signifying correlated orientations of the localized spins on the two impurities. This observation is consistent with Fig. 3(e) in the main text.

S6.4. Visualizing the evolution of RBM parameters

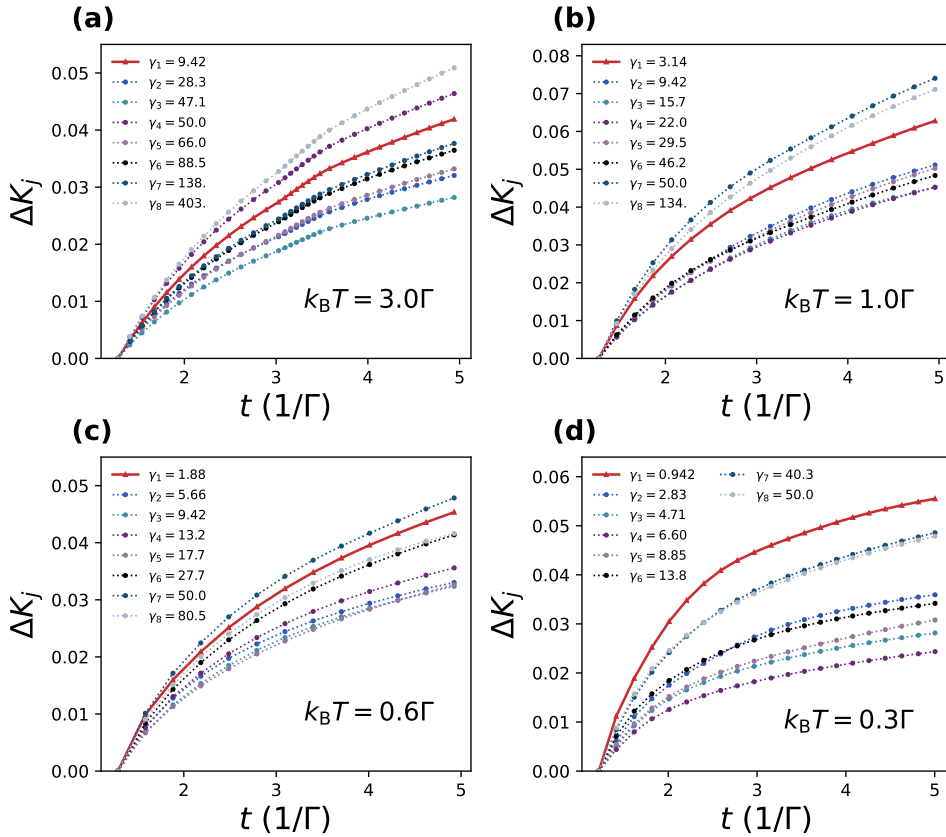


FIG. S4. Temporal evolution of auxiliary-layer-averaged weight per dissipaton level, ΔK_j , at various temperatures: (a) $k_B T = 3.0\Gamma$, (b) $k_B T = 1.0\Gamma$, (c) $k_B T = 0.6\Gamma$, and (d) $k_B T = 0.3\Gamma$. Here, the index j labels the decomposition index p in Eq. (S8), i.e., $\Delta K_j(t) = \frac{1}{N} \sum_{\alpha\nu a} |K_{\alpha\nu ja}(t) - K_{\alpha\nu ja}(t_{\text{sh}})|$ where the multi-index $\{\alpha\nu\}$ is the same as that in Eq. (S8) and a represents the auxiliary nodes. The $\Delta \mathbf{K}$ matrix in the main text is averaged only over multi-index $\{\alpha\nu\}$.

Figure S4 supplements Fig. 4 in the main text with additional intermediate temperatures. As the temperature decreases, the slowest-decaying dissipaton level progressively dominates

the long-time relaxation dynamics. This trend is clearly visible in Fig. S4, where the red line representing this level gradually becomes increasingly prominent among all lines.

S7. COMPARING THE PERFORMANCE OF NQS-DQME TO MPS-HEOM

Matrix product states (MPSs), a class of tensor network states (TNSs), have been used to provide compact representations of the dynamical variables (the RDO and ADOs) in the HEOM method [11]. In the MPS-HEOM approach, an ADO is approximated as

$$\rho_{\vec{m}}^{nn'} \approx \sum_{i_0, i_1, \dots, i_{N_E+2}} B_0(i_0, n, i_1) B_1(i_1, m_1, i_2) \cdots B_{N_E}(i_{N_E}, m_{N_E}, i_{N_E+1}) B_{N_E+1}(i_{N_E+1}, n', i_{N_E+2}), \quad (\text{S39})$$

where n and n' index system levels, \vec{m} labels the principal dissipation modes, and i_k (for $k = 0, 1, \dots, N_E + 2$) are the auxiliary tensor indices. The ranks of these tensors (the range of i_k) are the bond dimensions N_{bond} , which determine the number of dynamical variables in the MPS-HEOM method. Importantly, N_{bond} depends sensitively on both the strength of many-body correlations and the complexity of the non-Markovian memory in the OQS.

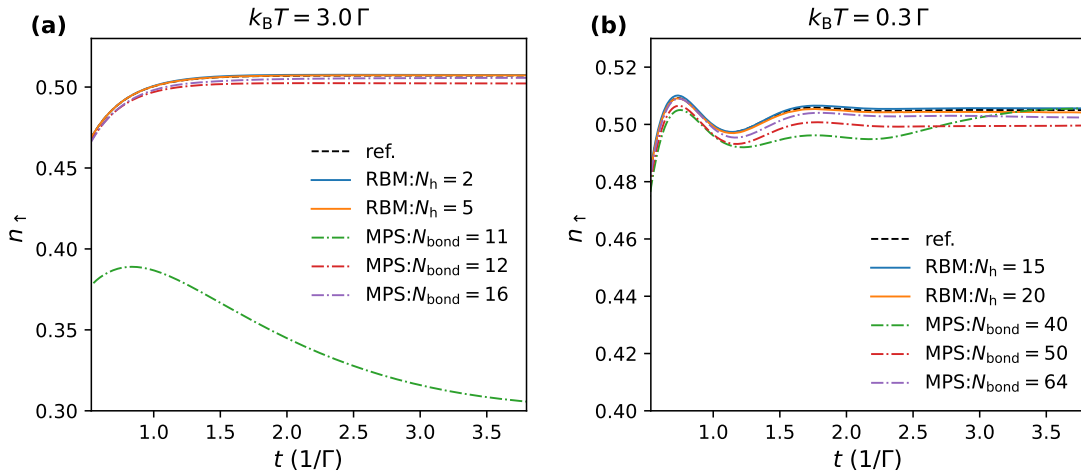


FIG. S5. Comparative performance of the MPS-HEOM and NQS-DQME methods for the single-impurity system (Case 1). Time evolution of the spin-up occupation number $n_{\uparrow}(t)$ at (a) high temperature ($k_B T = 3.0 \Gamma$) and (b) low temperature ($k_B T = 0.3 \Gamma$). Results from the NQS-DQME method with different numbers of hidden nodes (N_h) are compared with those from the MPS-HEOM method with different bond dimensions (N_{bond}). The NQS-DQME method achieves higher accuracy with significantly fewer parameters than the MPS-HEOM approach (see Table S11 for more details).

We now perform a direct comparison between the MPS-HEOM method [11] and our NQS-DQME approach by evaluating their performance in simulating the non-Markovian dynamics of the single-impurity Anderson model (Case 1).

Figure S5 presents a comparative analysis of the time evolution for the spin-up occupation number, $n_{\uparrow}(t)$, calculated by both methods at different temperatures. Panel (a) shows

TABLE S11. Comparison of parameter counts and accuracy for the MPS-HEOM and NQS-DQME methods in Case 1.

$k_B T/\Gamma$	3.0	0.3
$N_{\text{para (RBM)}}$	634 ($N_h = N_a = 2$, $\mathcal{E}_{n_\uparrow} = 0.07\%$)	5545 ($N_h = N_a = 15$, $\mathcal{E}_{n_\uparrow} = 0.11\%$)
$N_{\text{para (MPS)}}$	9184 ($N_{\text{bond}} = 12$, $\mathcal{E}_{n_\uparrow} = 0.81\%$)	299120 ($N_{\text{bond}} = 50$, $\mathcal{E}_{n_\uparrow} = 0.97\%$)
N_{RDT}	6724	51332

the high-temperature regime ($k_B T = 3.0 \Gamma$). The MPS-HEOM method requires a bond dimension of 12 (corresponding to 9,184 parameters) to achieve a truncation error of $\mathcal{E}_{n_\uparrow} = 0.81\%$. In contrast, the RBM within the NQS-DQME framework achieves a significantly lower error of 0.07% using only 634 parameters ($N_h = N_a = 2$).

This efficiency gap becomes even more pronounced at low temperatures, as shown in panel (b) for $k_B T = 0.3 \Gamma$. Here, MPS-HEOM requires a substantially larger bond dimension of 50 (299,120 parameters) yet yields a higher error of 0.97%. The RBM approach, with 5,545 parameters ($N_h = N_a = 15$), maintains superior accuracy with an error of only 0.11%.

The quantitative parameter counts and corresponding errors are summarized in Table S11. The data clearly demonstrates that the NQS-DQME method achieves higher accuracy with orders of magnitude fewer parameters than MPS-HEOM across both temperature regimes. This underscores the enhanced representational capacity and superior scalability of the RBM ansatz for capturing the complex non-Markovian dynamics of many-body OQs.

-
- [1] J. Hu, R.-X. Xu, and Y. Yan, *J. Chem. Phys.* **133**, 101106 (2010).
 - [2] J. Jin, X. Zheng, and Y. Yan, *J. Chem. Phys.* **128**, 234703 (2008).
 - [3] X. Li, S. Lyu, Y. Wang, R. Xu, X. Zheng, and Y. Yan, *Phys. Rev. A* **110**, 032620 (2024).
 - [4] M. J. Hartmann and G. Carleo, *Phys. Rev. Lett.* **122**, 250502 (2019).
 - [5] S.-C. T. Choi, C. C. Paige, and M. A. Saunders, *SIAM J. Sci. Comput.* **33**, 1810 (2011).
 - [6] C. J. Geyer, *Stat. Sci.* **7**, 473 (1992).
 - [7] N. Metropolis, A. W. Rosenbluth, M. N. Rosenbluth, A. H. Teller, and E. Teller, *J. Chem. Phys.* **21**, 1087 (1953).
 - [8] N. Roch, S. Florens, T. A. Costi, W. Wernsdorfer, and F. Balestro, *Phys. Rev. Lett.* **103**, 197202 (2009).
 - [9] J. Parks et al., *Science* **328**, 1370 (2010).
 - [10] X. Li et al., *Nat. Commun.* **11**, 2566 (2020).
 - [11] Q. Shi, Y. Xu, Y. Yan, and M. Xu, *J. Chem. Phys.* **148**, 174102 (2018).